Enhancing the thermo-mechanical properties of calcium aluminate concrete at elevated temperatures using synergistic flame-retardant polymer fibres

Tong Zhang[a,b,c], Mingzhong Zhang[c], Qing Chen[d], Hehua Zhu[a], Zhiguo Yan[a,*]

[a] State Key Laboratory of Disaster Reduction in Civil Engineering, College of Civil Engineering, Tongji University, Shanghai 200092, China

[b] School of Resources and Civil Engineering, Northeastern University, Shenyang, 110819, China

[c] Department of Civil, Environmental and Geomatic Engineering, University College London, London WC1E 6BT, UK

[d] Key Laboratory of Advanced Civil Engineering Materials of Ministry of Education, Tongji University, Shanghai 201804, China

Abstract: This paper presents a systematic study on the feasibility of using synergistic flame-retardant polymer (SFRP) fibres for enhancing thermo-mechanical properties of calcium aluminate concrete at elevated temperatures. A series of tests were conducted to investigate the effect of SFRP fibres and cement type on thermal conductivity, compressive, splitting and flexural behaviours, and microstructural and micromechanical evolutions of concrete at different temperature levels, based on which the underlying mechanisms for enhancing the thermo-mechanical properties of calcium aluminate concrete were explored. Experimental results indicate that the combined usage of calcium aluminate blinders and SFRP fibres can significantly promote the strength-sustaining capacity (e.g., less than 45% compressive strength loss at 800 $^{\circ}$C) and effectively prevent explosive spalling of concrete. The underlying mechanisms for enhanced thermo-mechanical properties of concrete can be explained by (i) the further reaction between hydration products and pozzolanic materials, which reduces the strength loss of concrete, and (ii) the melting, foaming and overflowing of SFRP fibres, which improves the connectivity of pore network and lowers the conductivity of concrete, and thereby improves the permeability and slows down the mechanical degradation of concrete.

Keywords: Calcium aluminate cement; Fibre reinforced concrete; Microstructural evolution; Fire resistance; Thermal analysis

1. Introduction

As an important class of non-Portland cementitious materials, calcium aluminate concrete (CAC) exhibits unique characteristics in terms of strength, durability and sustainability, making it favourable in numerous engineering applications such as castable refractories, sewer pipes, industrial floors and railway tunnels [1]. Due to the rapid hardening process induced by precipitation of ettringite, the compressive strength of CAC can reach over 60 MPa within 2 d [2], which can be well predicted based on the relationship between strength and porosity [3]. However, the hydration of calcium aluminate cement is highly temperature-dependent, which yields metastable hexagonal hydrates at lower than 20 $^{\circ}$C and converts to more stable hydrates at over 30 $^{\circ}$C [4]. Although CAC suffers a strength loss during conversion reactions, the addition of pozzolanic

admixtures (e.g., blast furnace slag, metakaolin, fly ash, and micro silica [5–7]) and reactive clinker aggregates (e.g., synthetic calcium aluminate aggregates [8,9]) are effective in reducing or eliminating the negative effect of conversion at different temperatures. Besides, calcium aluminates can be used as aggregates together with CAC binders, and thereby the reaction between aggregates and blended binders would lead to the continuity of phases and properties in the past-to-aggregate interfacial transition zone (ITZ) [10]. The dense ITZ in CAC can lead to superior durability, including slower carbonation and higher resistance to chloride ingress and abrasion [11] compared to ordinary Portland concrete (OPC). Moreover, the sulfuric acid reaction during hardening process of CAC can help slow down the mechanical degradation at lower PH levels, leading to the inherent resistance to alkali-silica reaction [6] as well as acid attack and biogenic corrosion [12]. The high efficiency (up to 53%) and permanent binding capacity of surface-related heterogeneous interactions between NO_x (nitrogen oxides) and aluminium-bearing hydrated phases also make CAC a potential candidate for NO_x sequestration in cementitious materials [13]. In addition, the decomposition products of CAC hydrates at elevated temperatures are stable or form stable compounds, which even results in a rise in strength at 450 ^{o}C due to the further hydration of CAC [14], enabling the development of fire-resistant high-performance concrete using calcium aluminate binders.

In addition to the innovation of cement binders, other methods to enhance the fire resistance of concrete includes: (i) To adopt a reasonable curing regime. The combined curing method composed of precuring in hot water and heating in dry air at 200 ^{o}C can not only activate further hydration of cement and pozzolanic reactions forming a denser microstructural framework but also consume most of the internal free water and prevent spalling occurrence of concrete at up to 800 ^{o}C [15–17]. (ii) To add different dimensions of aggregates or fillers [18,19]. Lightweight aggregates have higher efficiency than granite aggregates in promoting the residual strength of concrete after heat exposure because of the presence of voids which mitigate the thermal expansion stress in concrete [20]. Clinker aggregates help overcome the adverse conversion effect of CAC after exposure to 1000 ^{o}C for 1 h, which can be attributed to the increased hydration of calcium aluminate cement and the enhanced interlocking effect at the reactive aggregate interface [8]. (iii) To mix hybrid steel, polymer, and natural fibres. Various polymer fibres such as polypropylene (PP), polyethene (PE), polyvinyl alcohol (PVA) and recycled tyre fibres are effective in concrete spalling prevention [21–23], as the melting of polymer fibres creates pathways for the release of water vapour in concrete. Moreover, the thermal incompatibility between polymer fibres and concrete can help enhance the interconnected network of cracks and thus improves the permeability of concrete even before the melting of fibres [24,25]. In addition, the combined usage of polymer fibres and steel fibres or coarse aggregates has better performance in eliminating the spalling of concrete, because the microcracks generated by thermal expansion of steel fibres or coarse aggregates can further increase

2

the connectivity of empty tunnels left by polymer fibres [26]. Nevertheless, the enhancement effect of polymer fibres after phase changes might be greatly reduced, and the low-modulus of polymer fibres would inevitably weaken the mechanical properties of concrete [27,28].

In the authors' previous studies [29,30], a novel type of synergistic flame-retardant polymer (SFRP) fibre was developed and optimised by incorporating metallic-organic flame retardants into PP resin and its efficiency in mitigating the thermal damage of concrete was experimentally verified. This study aims to further achieve the synergistic improvement in thermo-mechanical properties of concrete at elevated temperatures, taking full advantages of the fire resistance of calcium aluminate binders and the flame-retardant performance of SFRP fibres. A series of experimental tests were conducted to systematically investigate the effects of cement type and SFRP fibre content on thermal conductivity, as well as uniaxial compressive, splitting tensile and flexural behaviour of concrete exposed to elevated temperatures up to 800 ºC. The microstructural evolution of SFRP fibre reinforced CAC was characterised using X-ray diffraction (XRD), thermo-gravimetric analysis (TGA), differential scanning calorimetry (DSC), electron probe micro analysis (EPMA), and mercury intrusion porosimetry (MIP), while the micromechanical properties of different phases in CAC were explored using nanoindentation. Based on the obtained experimental results, the underlying mechanisms for enhancing the thermo-mechanical properties and mitigating the thermal damage of CAC at elevated temperatures were discussed in detail.

2. Experimental program

2.1. Raw materials

Granular polypropylene with a density of 0.90 g/cm^3 was used as the polymer resin matrix of SFRP fibres. The organic flame retardants made up of ammonium polyphosphate, pentaerythritol, and melamine were adopted as the main intumescent agents. To improve the thermo-mechanical properties of polymer fibres, magnesium hydroxide and aluminium hydroxide were applied as metallic fillers. These chemicals are commercially available and used without further purification.

Apart from the P.I 52.5R ordinary Portland cement, two types of calcium aluminate cements with different alumina content of approximately 50% and 70% were separately applied to produce CAC mixtures. Silica powder and class F fly ash were used as pozzolanic materials, which can not only increase the packing density of concrete but also promote the formation of hydration products at elevated temperatures [14]. Calcined bauxite particles with a density of 2.65 g/cm^3 were added as fine aggregates. The chemical compositions and particle size distribution of these raw materials are presented in Table 1 and Fig. 1, respectively.

Table 1 Chemical compositions of cementitious materials and fine aggregate (wt%).

Type	SiO_2	CaO	MgO	Al_2O_3	Fe_2O_3	Na_2O	Others
OPC	20.84	65.73	3.08	5.21	3.25	0.96	0.93
CA50	2.28	39.76	2.19	52.61	1.75	0.14	1.27

CA70	0.54	27.02	0.27	70.34	0.62	0.07	1.14
SP	93.76	1.28	1.19	0.64	0.87	0.98	1.28
FA	61.45	1.64	1.07	28.13	4.92	1.25	1.54
Aggregate	26.74	1.77	5.61	60.28	3.83	0.11	1.66

Note: CA50–calcium aluminate cement with 50% content of alumina, CA70–calcium aluminate cement with 70% content of alumina, SP–silica powder, FA–fly ash.
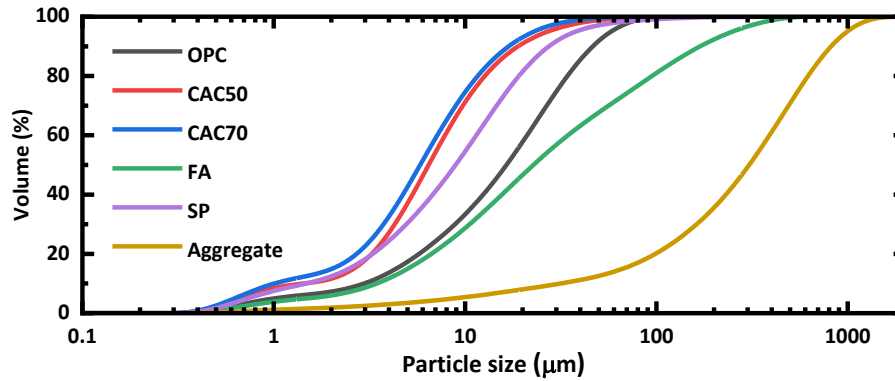

Fig. 1. Particle size distribution of raw materials.

2.2. Mix proportions

Based on the previous study [30], a type of synergistic flame-retardant polymer fibre was fabricated by embedding organic flame retardants and metallic fillers into polypropylene resin. The mix ratio between organic and metallic agents was carefully considered to achieve a balance between flame retardant efficiency and mechanical properties of polymer fibres [31,32]. In addition, stearic acid was incorporated as a non-toxic lubricant agent to facilitate the fabrication process. Table 2 provides the detailed mix proportion of SFRP fibre.

Table 2 Mix proportion of synergistic flame-retardant polymer (SFRP) fibre (wt%).

PP matrix	Organic flame retardants			Metallic intumescent fillers		SA
	APP	MEL	PER	$Mg(OH)_2$	$Al(OH)_3$	
50.00	10.7	10.7	5.3	8.9	4.4	10.00

Note: APP–ammonium polyphosphate, MEL–melamine, PER–pentaerythritol, SA–stearic acid.

Following previous studies [8,14], the mass ratio of cement, silica powder and fine aggregate was set as 1:0.25:1.5. Fly ash was used to replace 20% of cement to reduce the cement content and promote the pozzolanic reactions. Polycarboxylate superplasticizer (at 1.50% of cement by mass) was added to enhance the workability of concrete. In total, three types of cements, i.e., OP, CA50, and CA70 were considered, leading to three groups of plain OPC, CAC50, and CAC70. In addition, 2.0 vol% SFRP fibres were incorporated into concrete separately, resulting in three fibre reinforced mixtures. The water-to-binder ratio was kept consistent at 0.40 for all mixtures, the mix proportions of which are given in Table 3.

**Table 3** Mix proportions of plain and fibre reinforced OPC and CAC specimens.

Group	Cement type			Water	FA	SP	Aggregate	PBS	W/B	SFRP fibres (vol%)
	OPC	CA50	CA70							

OPC	0.80	–	–	0.50	0.20	0.25	1.50	0.012	0.40	–
FROPC	0.80	–	–	0.50	0.20	0.25	1.50	0.012	0.40	2.00
CAC50	–	0.80	–	0.50	0.20	0.25	1.50	0.012	0.40	–
FRCA50	–	0.80	–	0.50	0.20	0.25	1.50	0.012	0.40	2.00
CAC70	–	–	0.80	0.50	0.20	0.25	1.50	0.012	0.40	–
FRCAC70	–	–	0.80	0.50	0.20	0.25	1.50	0.012	0.40	2.00

Note: PBS–polycarboxylate superplasticizer, W/B–water-to-binder ratio.

2.3. Sample preparation

As per the previous studies [29,30], SFRP fibres were fabricated through melting extrusion and cooling moulding methods, as illustrated in Fig. 2. The solid mixture of raw materials after drying at 80 $^{\circ}$C for 2 h was poured into the feeding port and transformed into the heating sections by twin screws. Afterwards, the melt compounding and extrusion processes of the composites were performed on a co-rotating twin-screw extruder (HTGD-20, Hartek, China). The extruded needle-like polymer composites were then cooling moulded in a water sink and cut into a suitable length of around 10 mm using a pelletizer machine. The density and melting point of the fabricated fibres were approximately 1.41 g/cm^3 and 165 $^{\circ}$C, respectively.
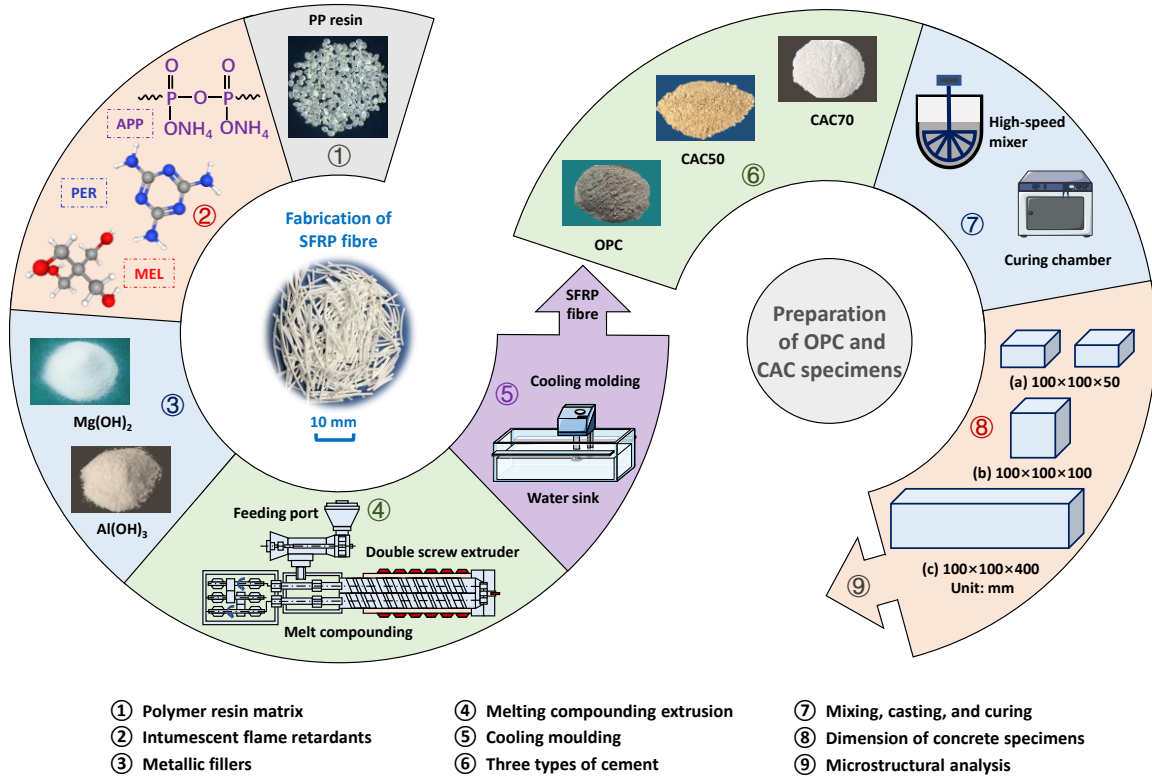
Fig. 2. Schematic illustration of the preparation of SFRP fibres and CAC specimens.

The mixing process of plain and fibre reinforced mixtures was performed as per GB/T 50081 [33]. The fresh mixtures were poured into oiled plastic moulds with dimensions of 100×100×100 mm^3 and 100×100×40 mm^3 to make specimens for thermal conductivity test and mechanical tests, including compressive strength, splitting tensile, and four-point bending tests. Then, all specimens were cured inside moulds for 24 h, after which they were demoulded and cured in a standard chamber (95% relative humidity and 20 $^{\circ}$C) for another 27 d. After the curing stage, some of the

cubic specimens were cut into two identical pieces for the measurement of thermal conductivity. Before the mechanical tests, the cubes and beams were exposed to elevated temperatures in a muffle furnace. The temperature of furnace was increased from 20 °C to target temperatures at a heating rate of 5 °C /min and maintained at that condition for 2 h, followed by naturally cooling down to the ambient temperature. The target temperature varies from 200 to 800 °C with an interval of 200 °C, except that of the bending test which changes from 300 to 600 °C. It is worth mentioning that a different exposure regime was adopted for the bending test to reflect the most significant variation in thermo-mechanical properties of CAC while simplifying the extensive experiment. Moreover, the weight of specimens before and after heat exposure was measured and recorded. Table 4 provides more details about the size, number and temperature conditions of all tested specimens.

Table 4 Details of the thermal and mechanical tests at elevated temperatures.

Test methods	Specimen size (mm^3)	Specimen number	Test temperature (°C)
Thermal conductivity test	100×100×50	6 (M)×5 (T)×2 (P)	20, 200, 400, 600, 800
Compressive strength test	100×100×100	6 (M)×5 (T)×3 (R)	20, 200, 400, 600, 800
Splitting tensile test	100×100×100	6 (M)×5 (T)×3 (R)	20, 200, 400, 600, 800
Four-point bending test	100×100×400	6 (M)×3 (T)×3 (R)	20, 300, 600

Note: M–mixture, T–temperature, R–replication, P–piece.

2.4. Test methods

2.4.1. Thermal conductivity test

The thermal conductivity of specimens was measured using a thermal constant analyser (Hot Disk, TPS-2500S, Sweden). During the test, two identical specimens (100×100×50 mm^3) fitted with a Mica plane sensor were placed in a muffle furnace [34]. The furnace was firstly heated up to 200 °C at a pace of 10 °C/min and maintained until thermal equilibrium. Then, the thermal conductivity of specimens was automatically measured and recorded, after which the furnace was heated up again to the next temperature. This procedure was continued to 800 °C. The conductivity measurement was repeated three times at each temperature to ensure the reliability of the measured results.

2.4.2. Compression test

After exposure to elevated temperatures (see Section 2.3), the residual compressive properties of specimens were measured using an electro-hydraulic servo testing machine (HUT305D, WANCE, China). Under the load-controlled mode, a constant loading rate of 0.20 MPa/s was adopted until the failure of tested specimen. In total, there were five temperature levels considered in the uniaxial compression tests as listed in Table 5. Additionally, three cubs with the same mix were tested for each temperature to obtain the average and standard deviation values of compressive strength.
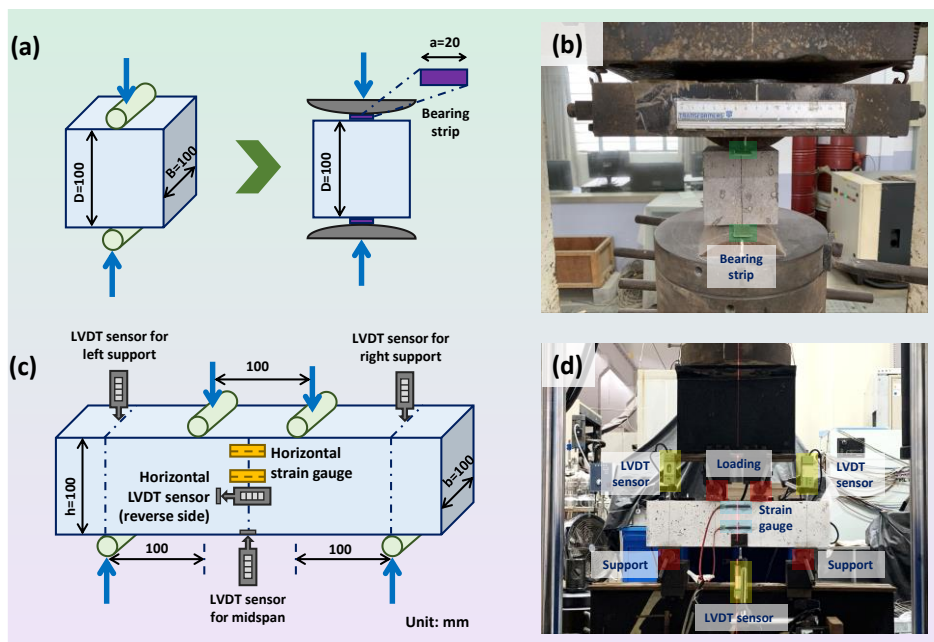
2.4.3. Splitting tensile test

Splitting tensile tests were conducted to measure the tensile properties of specimens after heat exposure. As illustrated in Fig. 3a and b, the cubic specimen with a side length of 100 mm was compressed along with two diametrically opposed generators. The test was performed under

deformation control with a constant loading rate of 0.01 mm/s, where the load was distributed through two bearing strips to prevent multiple cracking and local failure in compression [35]. The load-displacement curves were recorded, based on which the tensile strength was calculated.

2.4.4. Four-point bending test

To investigate the flexural behaviour after heating, four-point bending tests were carried out on OPC and CAC beams ($100 \times 100 \times 400$ mm^3 with a clear span length of 300 mm) according to ASTM C 1609 [36]. A universal testing machine was applied to perform the displacement-controlled uniaxial load at a rate of 0.2 mm/min as shown in Fig. 3c and d. Linear variable differential transducers (LVDT) and strain gauges were installed to measure the midspan deflection and transverse strain, respectively. Based on the obtained load-deflection curves, the peak-load toughness of beams can be calculated.

Fig. 3. Experimental setup of the preparation of splitting tensile and four-point bending tests.

2.4.5. X-ray diffraction

The XRD patterns of CAC samples after exposure to elevated temperatures were measured using an X-ray diffractometer (X'Pert, PANalytical, Netherlands) by employing CuKα radiation at 40 kV and 30 mA. The crystalline phases were scanned from a 2θ range of 10° to 70° with a scanning rate of 0.02 °/step and identified based on the standard PDF (powder diffraction file) database.

2.4.6. Thermal analysis

The thermal properties of samples extracted from fibre reinforced specimens were analysed through TG-DSC coupled measurement with the assistant of a thermal analyser (STA 449C, NETZSCH, Germany). Accurately weighted samples were loaded in a crucible and heated under a continuous N$_2$ atmosphere at a constant heating rate of 10 ºC /min from 20 ºC to 1200 ºC. The evolution of weight loss with temperature is reflected by TG curves and its first derivative curves (DTG), while DSC curves denote the heat transformation of physicochemical reactions.

7

2.4.7. Electron probe micro analysis

The element distribution of fibre reinforced samples after heating was measured using a micro electron probe (EPMA-1720, Shimadzu, China). Selected samples were cast in epoxy resin and polished until roughness was less than l mm, after which five main elements (i.e., Si, O, Ca, Al, and Mg) were detected and their distribution maps were plotted in terms of the weight percentage.

2.4.8. Mercury intrusion porosimetry

The pore size distribution of CAC samples was characterised using a mercury porosimeter (Auto Pore IV 9500, Micromeritics, USA) in the pressure range of 5 KPa to 350 MPa. Small pieces (< 0.5 cm^3) taken from retained cores after compression test were selected for each mixture. The mercury-solid contact angle of 130° was used for conversing pore radius through the Washburn equation [37].

2.4.9. Nanoindentation

The micromechanical properties of CAC samples after exposure to elevated temperatures were measured using a nanoindentation indenter (NHT, Anton Paar, Austria). The nanoindentation test started with linear loading under a constant rate of 5 mN/s until the maximum load of 50 mN. Then, the load at the maximum level was maintained for 5 s, followed by unloading at 5 mN/s. The load-displacement curves and images of indent impressions were obtained simultaneously.

3. Experimental results

3.1. Weight loss

Fig. 4 shows the weight loss of all specimens at elevated temperatures, in comparison with their weight at ambient temperature. In general, the weight loss of both OPC and CAC increases with the rising temperature and the incorporation of SFRP fibres speeds up the rate of weight loss. From 20 to 200 °C, the weight loss of all specimens fluctuates between 2.07% and 4.08% of the total weight, which can be attributed to the evaporation of free water and physically absorbed water. The decomposition of C–S–H in OPC and C–A–H in CAC takes place at over 100 °C, resulting in the release of chemically bound water in C–S–H and C–A–H gels [14]. The melting of PP resin in SFRP fibres at around 165 °C leaves more channels for moisture evaporation, leading to the higher weight loss of SFRP fibre reinforced specimens. When the temperature rises to 400 °C, the weight loss of plain OPC and CAC varies from 5.08% to 5.72% due to the evaporation of absorbed water and bound water. Moreover, the weight loss of FRCAC50 is 60.51% higher than that of CAC50 at 400 °C. This can be explained by the esterification among intumescent flame retardants of SFRP fibres, which enhances the pore structure of CAC matrix and facilitates the loss of moisture content [30]. At temperatures up to 600 °C, the weight loss of FRCAC50 and FRCAC70 increases significantly to 10.99% and 9.44%, respectively, which can be ascribed to the further loss of chemically bound water and the foaming reactions of SFRP fibres. It is worth noting that the linear expansion coefficient of SFRP fibres is over 10 times higher than that of CAC matrix [38]. Thus, the thermal expansion of SFRP fibres would generate micro pores/cracks along with the fibre

8

interfaces, which helps form the interconnected pore network for moisture evaporation [24] and thereby leads to a higher weight loss than plain CAC. When the temperature reaches 800 °C, the influence of SFRP fibres on weight loss of both OPC and CAC is pronounced. The weight loss of OPC shows a 23.33% increase while that of CAC70 has a 32.66% increase with the incorporation of 2.0 vol% SFRP fibres at 800 °C. The weight loss of CAC is less than OPC over the measured temperature range because of the improved thermal stability of microstructure in CAC [39].
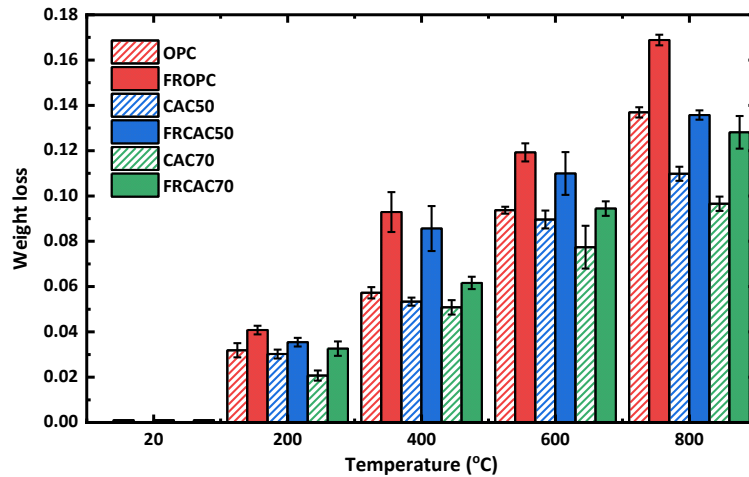
Fig. 4. Weight loss of plain and SFRP fibre reinforced OPC and CAC at elevated temperatures.

3.2. Thermal conductivity

The thermal conductivity of concrete is closely associated with the heat transfer and temperature distribution of composite structures at elevated temperatures [40]. Fig. 5 presents the variation of thermal conductivity with temperature for all specimens measured using the transient method. At ambient temperature, the thermal conductivity of CAC50 and CAC70 is 4.94% and 14.31% respectively higher than that of OPC induced by the higher conductivity of C–A–H gels (2.02–2.24 W/mK [41]) in CAC than that of C–S–H gels (0.74–1.25 W/mK [42]) in OPC. The addition of 2.0 vol% SFRP fibres leads to a 9.32% and 8.57% drop in thermal conductivity for FRCAC50 and FRCAC70, relative to that of plain CAC. This can be explained by: (i) The thermal conductivity of SFRP fibres (0.26–0.36 W/mK [30]) is much lower than that of CA mineral and C–A–H phases, which have an insulting effect on thermal properties of CAC [19,40]. (ii) The additional interfacial transition zones between SFRP fibres and CAC matrix would lead to an increased porosity [43] and thus a lower thermal conductivity by insulting of pore structure (0.026 W/mK [34]).

Fig. 5b displays the normalised thermal conductivity of all specimens at elevated temperatures, where a downward trend can be observed regardless of the cement type and fibre content. In general, the relationship curves between thermal conductivity and temperature can be roughly divided into two stages, i.e., a significantly decreasing stage before 200 °C, followed by a gently descent stage up to 800 °C. At 200 °C, the thermal conductivity of OPC and CAC70 reduces to 0.731 and 0.791 of that at 20 °C, due to the loss of free and absorbed water as well as the dehydration of C–S(A)–H gels [14]. In contrast, FROPC and FRCAC70 exhibit a 33.61% and 25.59% decrease in thermal

conductivity with the increasing temperature from 20 °C to 200 °C, indicating that besides the loss of moisture, other factors accelerate the decrease in thermal conductivity. In addition, SFRP fibres start to melt at around 165 °C, implying that the additional gaps left by softening and melting of SFRP fibres can lead to higher porosity and accordingly lower the thermal conductivity [22]. When the temperature is over 200 °C, the continuous decomposition of C–A–H phases and loss of chemically bound water cause a relatively linear decrease in thermal conductivity. Noted that the metallic-organic flame retardants in SFRP fibres would experience complex foaming reactions at the temperatures of 220–490 °C [30], which not only promotes the connectivity of pore structure but also reduces the thermal conductivity. Consequently, the thermal conductivity of FRCAC50 and FRCAC70 is 15.53% and 16.68% lower than that of CAC50 and CAC70 at 400 °C, respectively. Moreover, the drop in thermal conductivity of SFRP fibre reinforced CAC is steeper than that of plain CAC, indicating that the effect of SFRP fibres is enhanced during this stage.
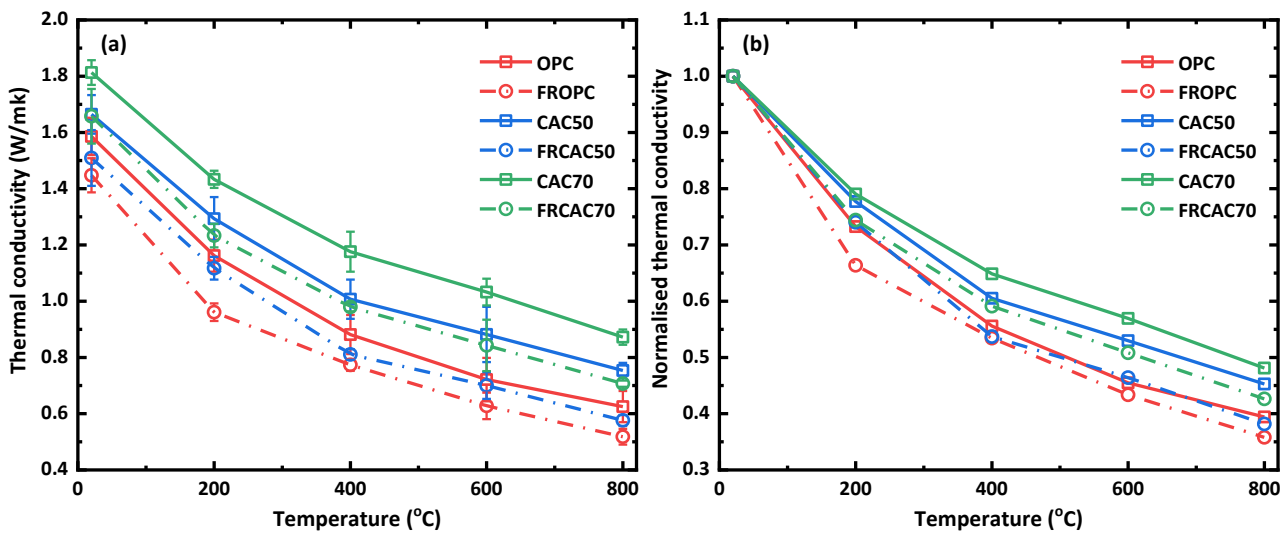

Fig. 5. (a) Thermal conductivity of plain and SFRP fibre reinforced OPC and CAC, and (b) the normalised form of conductivity at elevated temperatures.

3.3. Compressive strength

The uniaxial compressive strength of plain and fibre reinforced specimens against temperature is plotted in Fig. 6 and Fig. S1. At 20 °C, the compressive strength of CAC50 and CAC70 is 4.86% and 18.81% higher than that of OPC, which is consistent with the previous study that the strength of CAC is 6.96% and 12.75% higher than that of OPC after curing for 14 d and 28 d [39]. Although the hydration of CAC is highly temperature-dependent, the intensive hardening of CAC releases 70%–90% of the total hydration heat in the first 24 h curing, leading to the higher early strength of CAC than OPC [44]. The incorporation of 2.0 vol% SFRP fibres results in a 1.39% increase in the compressive strength of OPC, while a 2.06% and 1.28% drop in compressive strength can be observed for CAC50 and CAC70, respectively. In general, the addition of polymer fibres, i.e., PP and PVA fibres, would cause a decrease in concrete strength due to their low modulus. For instance, the addition of about 0.65 vol% PP fibres results in a 5.44% strength loss of UHPC [26]. It is noted

that if the SFRP fibres are modified with high-modulus metallic fillers, their mechanical properties (e.g., adhesion and elastic modulus) can be improved [30]. Therefore, SFRP fibres have an insignificant effect on the compressive strength of OPC and CAC at ambient temperature.
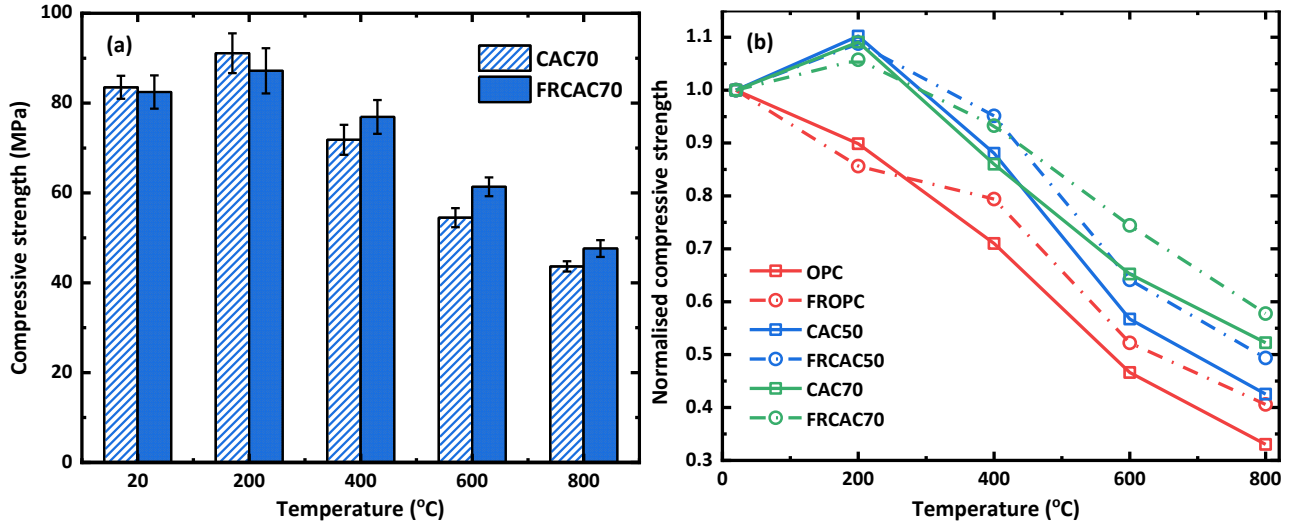
Fig. 6. Compressive strength of (a) CAC70 and FRCAC70 at elevated temperatures, and (b) the normalized form of strength.

Fig. 6b shows the normalised compressive strength of all specimens at elevated temperatures. Overall, the compressive strength of OPC decreases continuously with increasing temperature, while that of CAC reaches the maximum value at 200 °C and then decreases with a further increase of temperature. The reduction in compressive strength of OPC can be mainly attributed to the continuous dehydration of C–S–H gels from 120 °C to 640 °C, dehydration of CH crystals in the temperature range of 400–530 °C, and decomposition of $CaCO_3$ at over 530 °C [45]. Different from OPC which suffers from a 10.14% drop in compressive strength at 200 °C, the compressive strength of CAC50 and CAC70 is increased by 10.21% and 9.09%, respectively. A previous study found that CAC even has a 24.06% increase in strength after exposure to 200 °C for 1 h [8]. The abnormal strength increase can be explained by the conversion reactions in CAC, which promote the mechanical interlocking effect between fine aggregates and cement paste [8,39]. Although the compressive strength of FRCAC also goes up when the temperature rises from 20 °C to 200 °C, the strength of FRCAC50 and FRCAC70 is 3.31% and 4.31% lower than that of plain CAC at 200 °C, respectively due to the melting and softening of SFRP fibres at 165 °C [30]. As the temperature increases, the compressive strength of CAC70 is reduced to 0.860 at 400 °C and 0.652 at 600 °C, respectively relative to that at ambient temperature, which can be ascribed to the dehydration of aluminium hydroxide phases from 210 °C to 300 °C, decomposition of C_3AH_6 between 240 °C and 370 °C, and dehydration of $C_{12}A_7$ at over 400 °C (see Section 3.6 for more details). In addition, the compressive strength of FRCAC70 is about 7.07% and 12.61% higher than that of CAC70 at 400 °C and 600 °C, respectively. This is because the insulting flame retardants produced by foaming of SFRP fibres over 220–490 °C can overflow to the pore space of CAC matrix [29], which slows

11

down the heating rate of concrete and the degradation of strength. When the temperature reaches 800 ℃, the residual compressive strength of FROPC is about 0.406 of that at 20 ℃, while those of FRCAC50 and FRCAC70 are found to be 0.494 and 0.578, respectively. This can be attributed to the dense microstructure of C–A–H gels with better thermal stability [39], as well as the further carbonation of SFRP fibres at over 600 ℃, which leads to the formation of a local insulation layer over the fibre interface and thus mitigates the strength loss [29]. In addition, the strength evolution of CAC observed in this study is not consistent with that reported in a previous study [14] where the rise in strength of CAC50 can be observed at up to 450 ℃. The difference can be attributed to the inhibited conversion reactions of calcium aluminate hydrates at a low w/c ratio of 0.2 and the promoted formation of amorphous or semi-crystalline C-A-S-H gels by micro silica at elevated temperatures [14].

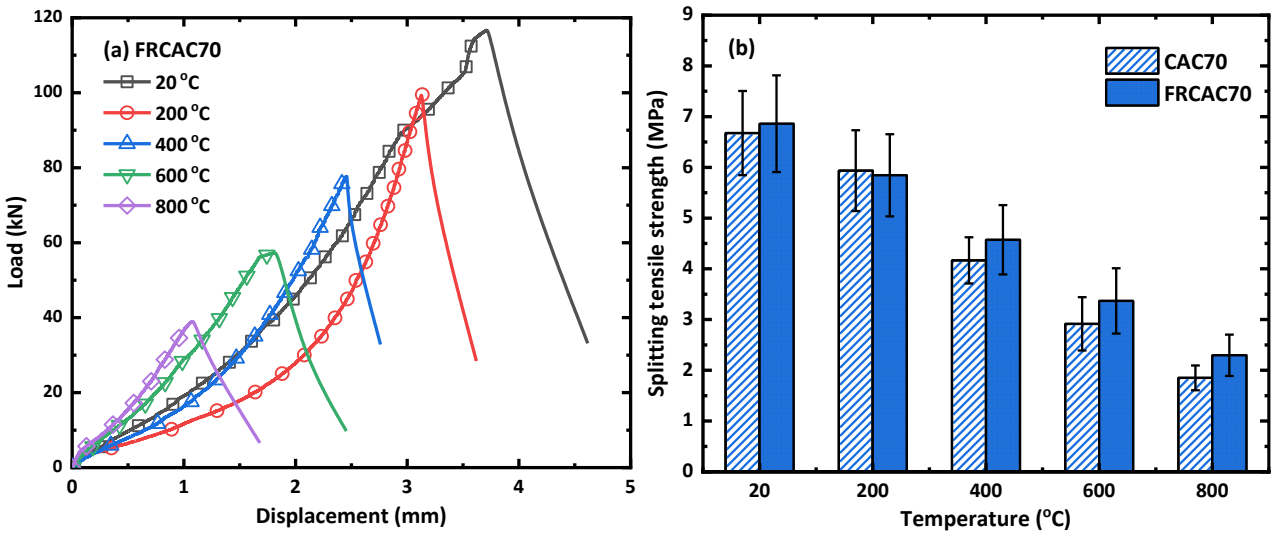## 3.4. Splitting tensile strength

3.4.1 Failure mode

Fig. 7 shows the evolution of splitting failure modes of fibre reinforced specimens with temperature. Clearly, all specimens present a brittle behaviour under splitting tension, since the first microcrack propagates throughout the specimen forming an interconnected network of microcracks which finally develops to a shear plane in the vertical direction until failure. At ambient temperature, it can be observed that some SFRP fibres are pulled out along the shear plane, which can contribute to the tensile behaviour of CAC through the pull-out effect of fibres [46]. At elevated temperatures, the physicochemical reactions of SFRP fibres have no direct influence on the failure mode of CAC.
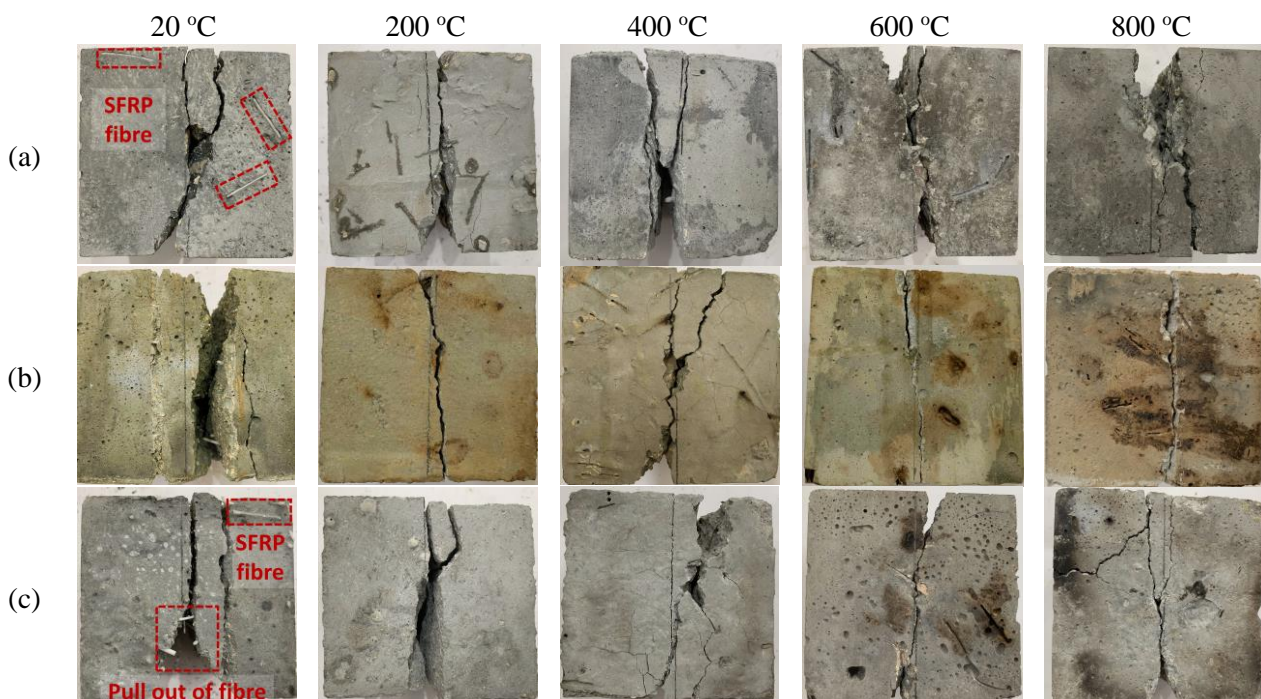
Fig. 7. Failure mode of (a) FROPC, (b) FRCAC50, and (c) FRCAC70 under splitting tension.

3.4.2 Load-displacement response

The splitting load-displacement curves of fibre reinforced specimens shown in Fig. 8a and Fig. S2 provide more insights into the effect of SFRP fibres. In general, the typical splitting load-displacement includes an increasing stage reaching the peak load and a decreasing stage approaching a relatively low value of the residual stress. Although the slop of increasing stage increases with temperature, both the peak load and the corresponding displacement decrease significantly when the temperature rises, regardless of the types of cement. For instance, the peak load of FRCAC50 decreases from 90.07 kN to 54.94 kN, and the displacement at peak load also drops from 2.89 mm to 1.52 mm with the rising temperature from 200 °C to 600 °C, indicating that the specimen becomes more brittle due to the evaporation of moisture and dehydration of C–A–H gels. Additionally, compared to FRCAC, FROPC suffers more in the degradation of peak load with temperature, which can be estimated using the residual tensile strength in the following section.

Fig. 8. (a) Splitting load-displacement curves of FRCAC70, and (d) splitting tensile strength of CAC70 and FRCAC70 at elevated temperatures.
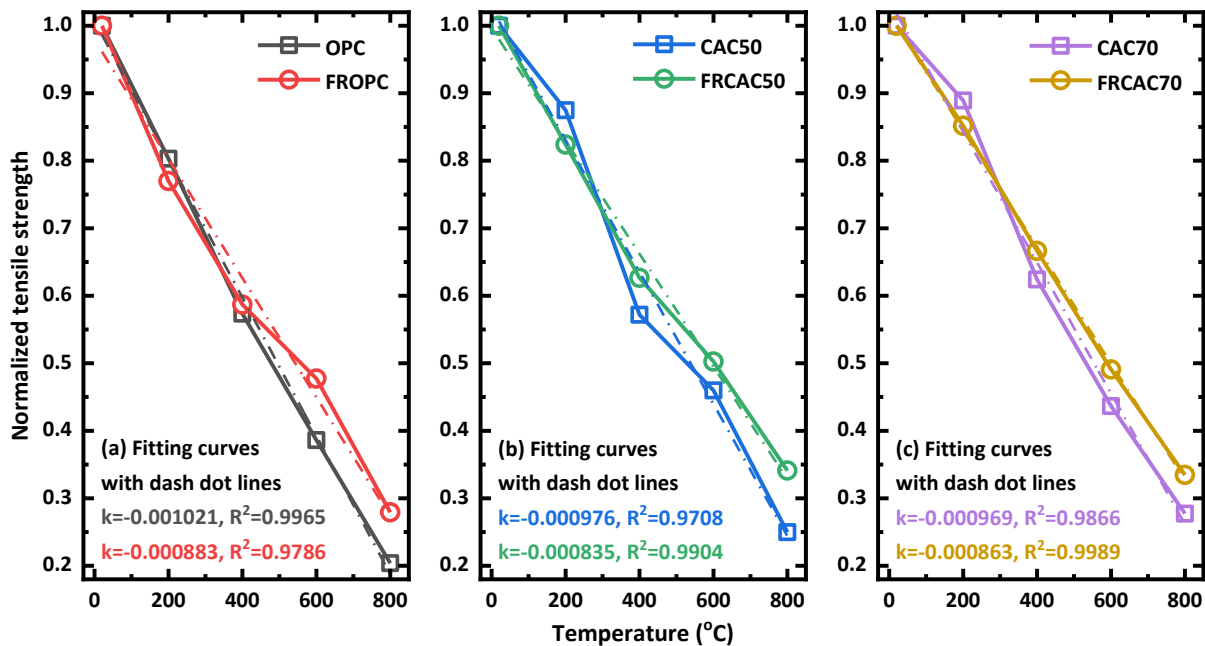
3.4.3 Splitting tensile strength

Based on the load-displacement curves from the standard splitting test, the tensile strength (f_t) of cubic specimens can be calculated taking into account the effect of specimen geometry and the relative width of load-bearing strips as [35]:

$$f_t = \frac{2P_u}{\pi BD}\left[\left(1-\eta^2\right)^{5/3}-0.0115\right]^{-1} \tag{1}$$

where P_u is the peak load of load-displacement curve, B and D are the specimen depth and thickness, respectively, and $\eta = a/D$ denotes the relative width of the strips as illustrated in Fig. 3a.

The obtained splitting tensile strength of plain and fibre reinforced specimens is plotted as a function of temperature in Fig. 8b and Fig. S2. At 20 °C, the tensile strength of OPC and CAC is almost the same (i.e., 6.18–6.198 MPa), while that of CAC70 is 6.68 MPa, indicating a promoting effect of alumina content on splitting tensile strength of CAC. The incorporation of SFRP fibres

results in a 2.84% and 3.75% increase in the splitting tensile strength of CAC50 and CAC70, respectively, because of the crack-bridging effect of SFRP fibres. Consistent with a previous study [39], the tensile strength of both OPC and CAC shows a downward trend with elevated temperatures, unlike the compressive strength of CAC which reaches a maximum value at 200 °C. The normalised splitting tensile strength displayed in Fig. 9 suggests that OPC is more vulnerable to thermal degradation than CAC as the relative tensile strength of OPC is only 0.364 at 600 °C in comparison with that of CAC50 (0.460). The slop of fitting curves also reflects the degradation trend of tensile strength with temperature. As seen in Fig. 9, the relative slope for CAC50 is 9.79×10^{-4} while that for FRCAC50 is 8.35×10^{-4}, indicating that the addition of SFRP fibres mitigates the strength loss of CAC. This can be ascribed to the physical and chemical changes of SFRP fibres at elevated temperatures, including melting (at 165 °C), foaming (220–490 °C), overflowing and char formation (at over 600 °C) [29,30], which slows down the heating rate of specimens and the degradation of tensile strength. Moreover, the incorporation of SFRP fibres in CAC70 is the optimal choice in terms of the tensile strength at ambient temperature and strength loss with temperatures.


Fig 9. Linear regression of normalised splitting tensile strength of plain and SFRP fibre reinforced OPC and CAC at elevated temperatures.

3.4.4 Relationship between compressive and tensile strengths

The tensile strength of OPC and CAC is much lower than the compressive strength, largely due to the ease with which a single flaw or microcrack can propagate rapidly under tensile loads. However, there is a close relationship between compressive and tensile strengths, as compressive strength can be adopted to predict the splitting tensile strength of concrete [47]. Fig. 10 demonstrates the compressive and tensile strengths of all specimens, where the points from top right to bottom left

represent the increase of temperature. Obviously, the relationship between two kinds of strength can be well fitted with linear regression, suggesting a similar change trend of both strengths with elevated temperatures. The slope of compressive-tensile strength fitting curves of CAC50 decreases from 0.085 to 0.075 with the addition of fibre, while that of CAC70 rises from 0.093 to 0.096. This suggests that SFRP fibres contribute more to mitigating the reduction in compressive strength with temperature for CAC50, while FRCAC70 performs better in terms of residual tensile strength. In other words, although both the compressive and tensile strength of FRCAC70 is improved in comparison with that of CAC70, SFRP fibres are more effective in retaining the compressive strength of concrete at elevated temperatures.
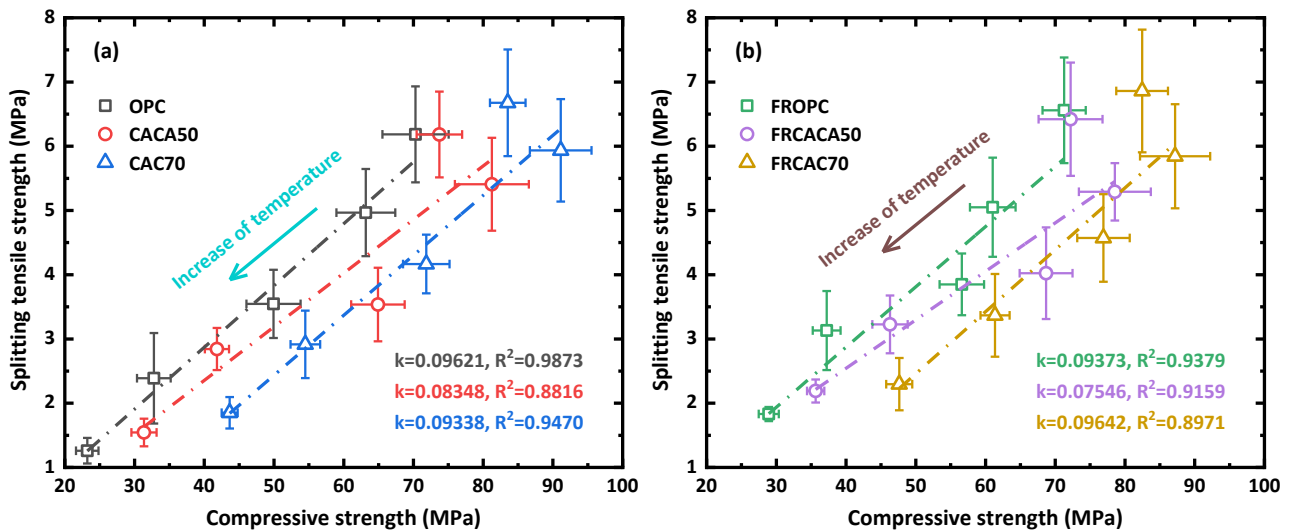

Fig. 10. Linear regression of compressive strength and splitting tensile strength of (a) plain specimens and (b) fibre reinforced specimens at elevated temperatures.

3.5. Flexural properties

3.5.1. Spalling behaviour

Fig. 11 illustrates the appearance of OPC and fibre reinforced specimens at elevated temperatures. The explosive spalling occurs in plain OPC when exposed to 600 ^{o}C, but no spalling can be observed in fibre reinforced specimens due to the enhanced permeability. On one hand, the high thermal expansion coefficient of polymer fibres gives an advantage of creating microcracks even before the melting of SFRP fibres [25]. On the other hand, the foaming reactions of SFRP fibres at over 200 ^{o}C would further enhance the pore structure of cement paste and promote the spalling resistance of concrete [30]. Moreover, the produced flame-retardant products driven by the thermal expansion of SFRP fibres can overflow through the interconnected pores, leading to the formation of a local insulation layer on the surface of specimens, as shown in Fig. 11c–d. Interestingly, CAC50 turns to dark yellow while the colour of CAC70 changes to light grey with the increase of temperature as a result of the major chemical changes [39]. The former can be ascribed to the decomposition of calcium aluminate hydrates from CAH_{10} to C_3AH_6 at 100 ^{o}C and finally forming $C_{12}A_7$ at 450 ^{o}C, while the latter can be associated with the formation of semi-crystalline C–A–H

gels through the further hydration of anhydrous CAC [14].
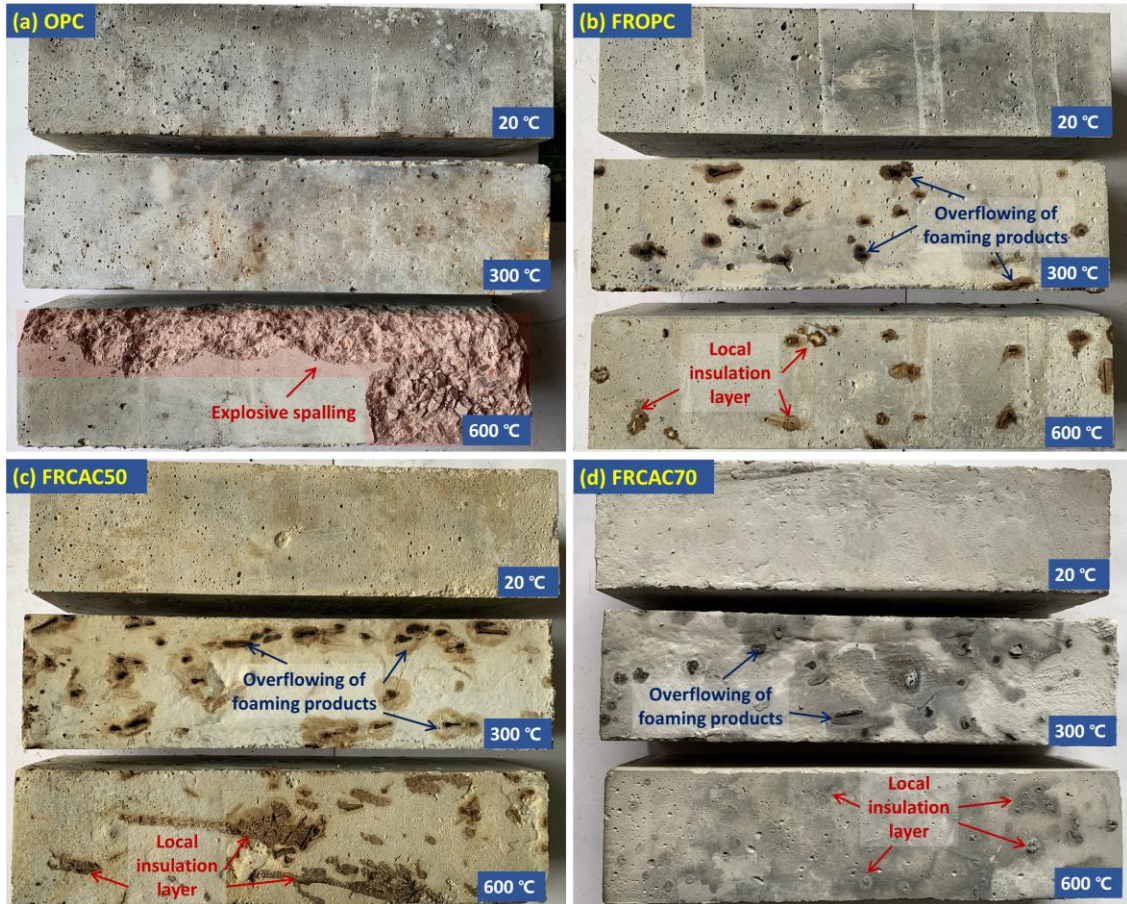
Fig. 11. Appearance of (a) OPC and (b)–(d) fibre reinforced specimens at elevated temperatures.

3.5.2 Load-deflection response

Fig. 12a and Fig. S3 display the load-deflection curves as well as the measured transverse strain (perpendicular to mid-span in Fig. 3b) of fibre reinforced specimens under four-point bending conditions. In general, the load-deflection curves include a rising stage with accelerated speed and a dramatic drop stage after reaching the maximum load, showing a typical failure pattern of brittle materials. The evolution of transverse strain with deflection is similar to that of load-deflection response. With the increase of temperature, both the maximum load and the corresponding deflection drop significantly, indicating the degradation of flexural properties with temperature. For instance, the maximum load of FRCAC50 decreases from 15.48 kN to 6.54 kN, while the deflection at peak load drops from 0.744 mm to 0.416 mm when the temperature increases from 300 $^{\circ}$C to 600 $^{\circ}$C. FRCAC70 performs the best in terms of residual peak load at 600 $^{\circ}$C, which is 45.31% and 23.26% higher than that of FROPC and FRCAC50, respectively. Moreover, the dramatic drop stage turns out to be a gradual decreasing stage in the load-deflection curves of specimens after exposure to 600 $^{\circ}$C, suggesting the deflection-softening response of CAC at elevated temperatures [48].
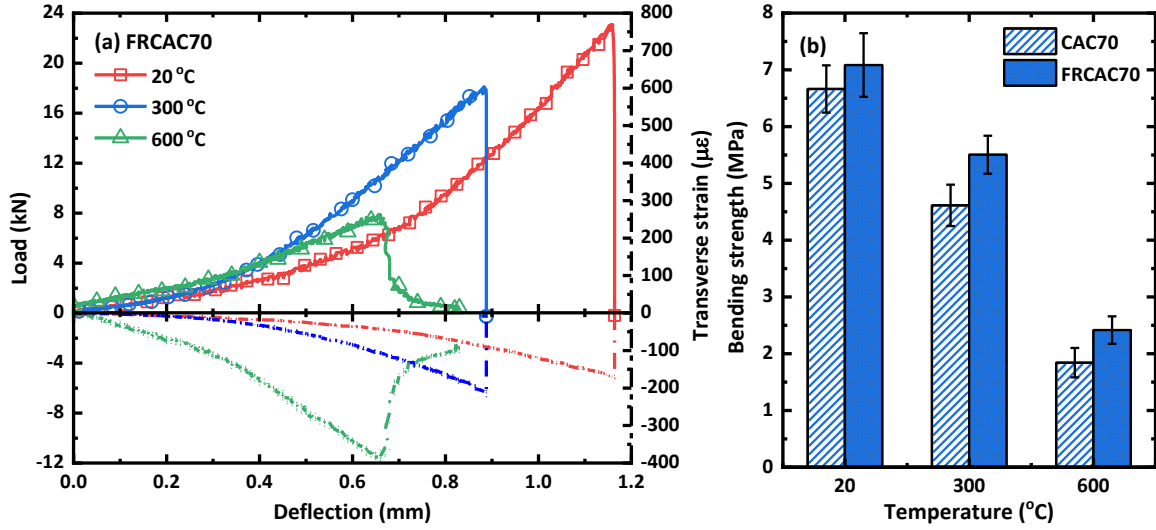
Fig. 12. (a) Flexural load-deflection curves of FRCAC70, and (b) flexural strength of CAC70 and FRCAC70 at elevated temperatures.

3.5.3 Bending strength

Based on the flexural load-deflection curves, the bending strength (f_{bs}) can be calculated by [36]:

$$f_{bs} = \frac{P_1 L}{bh^2} \tag{2}$$

where P_1 is the first-crack load at which the load-deflection curve has a change in gradient, L is the span length, and b and h denote the width and height of the tested specimen, respectively (Fig. 3b).

The calculated bending strength of plain and fibre reinforced specimens is plotted as a function of temperature in Fig. 12b and Fig. S3. Similar to that of splitting tensile strength, CAC70 exhibits the highest bending strength of 6.66 MPa at ambient temperature, which is 7.91% higher than that of CAC50. Although the effect of polymer fibre on bending strength of concrete highly depends on fibre content [49], there is an increase in bending strength by incorporating SFRP fibres, regardless of the cement type. FRCAC70 has the highest strength improvement of 6.34% in comparison with CAC70. The bending strength of all specimens drops with the increase of temperature in a similar manner to tensile strength, which is closely related to the removal of water and decomposition of hydrated products. The bending strength of CAC50 is reduced from 4.06 MPa to 1.57 MPa, while that of FRCAC50 decreases from 4.65 MPa to 1.96 MPa with the increasing temperature from 300 °C to 600 °C. The normalised bending strength plotted in Fig. 13 further suggests that the addition of SFRP fibres slows down the loss of bending strength with temperature as indicated by the decrease in slope of linear fitting curves. FRCAC70 performs the best in terms of residual bending strength, which is 0.777 at 300 °C and 0.341 at 600 °C relative to the strength at 20 °C. This can be ascribed to the thermal resistance of CAC70 and the thermal damage mitigation by SFRP fibres. Compared with the evolution of tensile strength with temperature, the degradation speed of bending strength at elevated temperatures is faster since the fitting curves in Fig. 13 are steeper than that in Fig. 9 under the same mix proportion. Thus, it can be indicated that the addition of steel fibres, i.e.,

hybrid steel and polymer fibres, might be more effective in further improving the flexural properties of CAC [50].
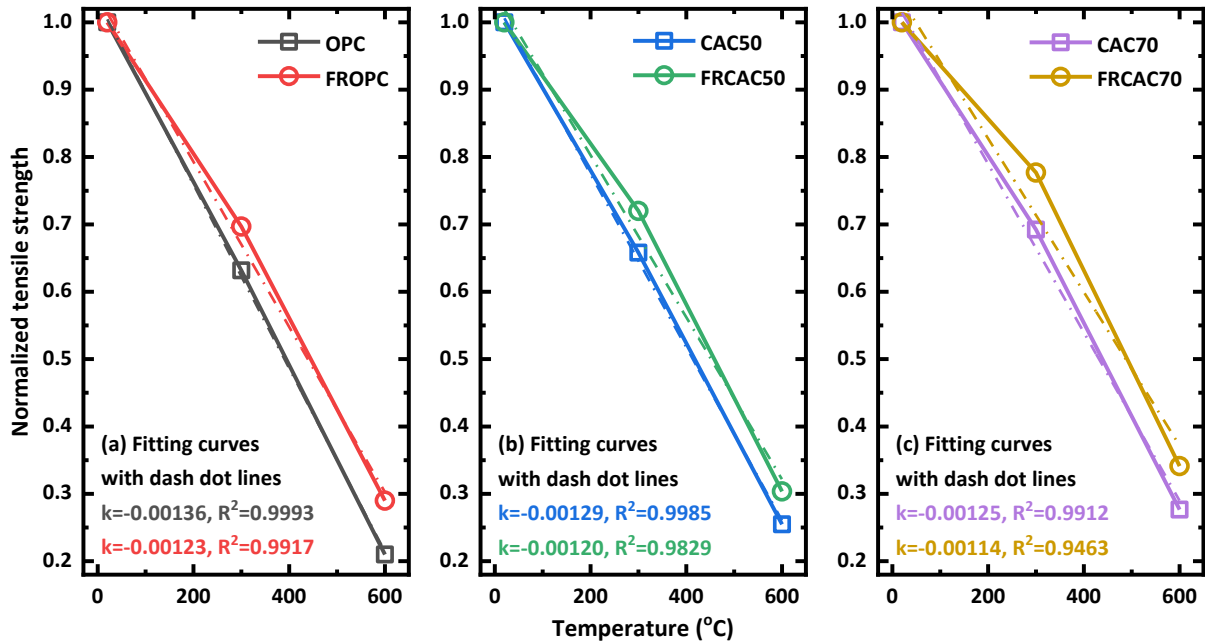
Fig 13. Linear regression of normalised flexural strength of plain and SFRP fibre reinforced OPC and CAC at elevated temperatures.

3.5.4 Peak-load toughness

The peak-load toughness is defined as the area under the load-deflection curve up to the deflection at peak load [51], which can be used to estimate the energy absorption capacity. Table 5 lists the toughness of all specimens and their normalised values relative to the toughness at 20 $^{\circ}$C. Similar to that of bending strength, the peak-load toughness also decreases with increasing temperature, while the incorporation of SFRP fibres mitigates the toughness loss. In addition, FRCAC70 shows the highest capacity of energy absorption at all measured temperature levels, the toughness of which is 16.02% and 41.30% higher than that of FRCAC50 at 20 $^{\circ}$C and 600 $^{\circ}$C, respectively.

Table 5 Peak-load toughness of OPC and CAC beams after exposure to elevated temperatures

Specimen number	20 $^{\circ}$C		300 $^{\circ}$C		600 $^{\circ}$C	
	T_{peak} (N·m)	Relative	T_{peak} (N·m)	Relative	T_{peak} (N·m)	Relative
OPC	6.34±0.75	1.00	1.96±0.22	0.31	0.66±0.08	0.11
FROPC	6.91±1.07	1.00	2.63±0.49	0.38	1.11±0.24	0.16
CAC50	6.75±0.89	1.00	3.72±0.41	0.55	1.33±0.16	0.20
FRCAC50	7.29±0.99	1.00	4.92±0.57	0.67	1.83±0.28	0.25
CAC70	7.09±0.75	1.00	4.50±0.53	0.66	1.76±0.24	0.25
FRCAC70	8.46±0.89	1.00	5.75±0.64	0.68	2.58±0.31	0.31

As seen in Fig. 14, the evolution of toughness is closely related to the crack distribution of beams under four-point bending. In general, most of the cracks are located in the middle part of the beams. At ambient temperature, SFRP fibres help bridge the cracks and impart ductility to the composite as many microcracks develop from the bottom of beams, especially for FRCAC70. This is consistent with the results in a previous study [49] that polymer fibres would improve the crack

resistance of concrete and induce multiple microcracks. However, the fibre reinforced concrete beams gradually lose their toughness and ductility at 300 °C, resulting in a major macrocrack that causes the failure of tested beams. Although SFRP fibres might not directly enhance the crack behaviour due to the phase transformation, they can still contribute to the toughness of CAC beams by restraining the mechanical degradation of concrete.
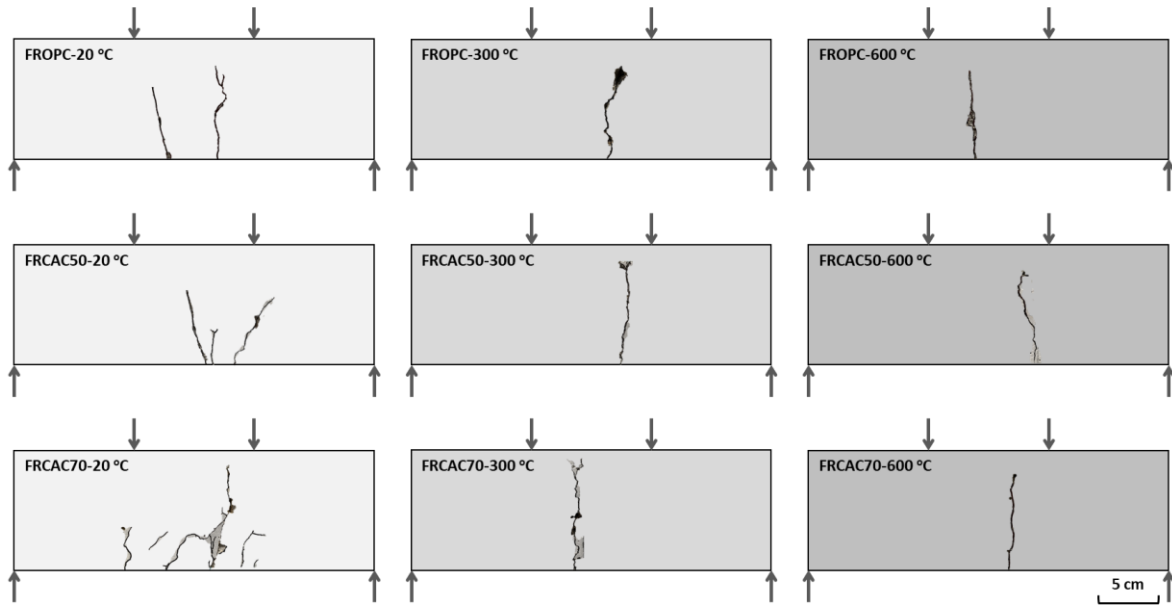

Fig. 14. Crack distribution of fibre reinforced concrete specimens under four-point bending.

3.6. Microstructural evolution

3.6.1. Phase composition

Given that most hydration products of CAC are completely dehydrated before 400 °C [18], Fig. 15 compares the XRD patterns of fibre reinforced CAC samples at 400 °C with that at ambient temperature. The hydration of CA (Al_2CaO_4), as the main hydraulic cement minerals in CAC, leads to the formation of calcium aluminate hydrate CAH_{10} ($CaAl_2O_{14}H_{20}$) at lower than 20 °C, while C_2AH_8 ($Ca_2Al_2O_{13}H_{16}$) and aluminium hydroxide (AH_3) are formed at temperatures between 20 °C and 30 °C [7]. However, the two first hexagonal hydrates are chemically metastable and suffer a conversion to the more stable compounds C_3AH_6 ($Ca_3Al_2O_{12}H_{12}$) and AH_3 at over 55 °C, which is highly dependent on humidity and temperature [4]. As illustrated in Fig. 15a, the main crystalline phase at ambient temperature is CAH_{10} in FRCAC50, while the peaks of C_2AH_8 and AH_3 are rarely detected as the hydration of CAC takes place at 20 °C. In addition, some peaks of C_3AH_6 are detected, which can be attributed to the conversion reactions during curing period. After exposure to 400 °C, the peaks corresponding to CAH_{10} disappear while the presences of AH_3 and $C_{12}A_7$ ($Ca_{12}Al_{14}O_{33}$) are newly detected, which can be associated with the dehydration of CAH_{10} and C_3AH_6 [8]. Besides, the peaks related to C_2ASH_8 ($Ca_2Al_2SiH_{16}O_{15}$) are also observed at 400 °C. The formation of semi-crystalline C–A–(S)–H gels can be ascribed to the further hydration of CAC with pozzolanic materials and thereby contributes to the high strength-sustaining capability of CAC at

elevated temperatures [14]. The XRD diffraction patterns of FRCAC70 (Fig. 15b) resemble that of FRCAC50 only with some fluctuations of intensity at peaks. Moreover, the incorporation of SFRP fibres has no significant influence on the phase composition of CAC, which is confirmed by a previous study [25] that polymer fibres do not affect the hydration of cement.
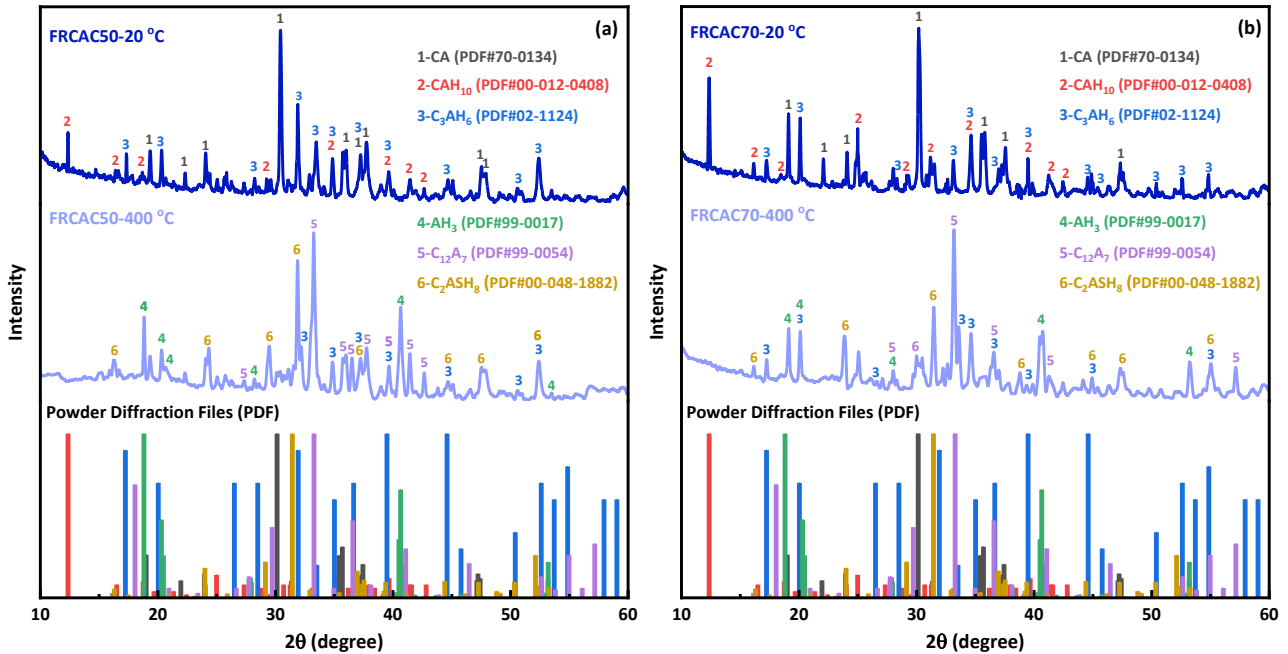

Fig. 15. X-ray diffraction patterns of fibre reinforced CAC samples at 20 °C and 400 °C.

3.6.2. Thermal analysis

Fig. 16 illustrates the thermal analysis results of fibre reinforced specimens in terms of TG, DTG and DSC curves. For the FROPC sample (Fig. 16a), there exists a rapid loss of restrained weight at around 100 °C due to the evaporation of free water. Then, both DTG and DSC curves show a sudden drop between 400 °C and 500 °C, which can be associated with the removal of physically absorbed water and chemically bound water from C–S–H phases and the decomposition of calcium hydroxide (CH) into calcium oxide, respectively [22]. It is noted that most of the moisture content is lost at 600 °C as 85.84% of the total mass loss occurs before this temperature. In addition, some fluctuations of the DSC curve occur in the ranges of 700–800 °C, attributing to the dissociation of calcium carbonate [52]. For FRCAC samples (Fig. 16b and c), there are several drops of DTG and DSC curves from 100 °C to 300 °C, which can be explained by the dehydration of C–A–H gels. According to a previous study [53], CAH_{10}, C_2AH_8, and C_3AH_6, as three typical types of C–A–H phases, dehydrate at the temperatures of 120 °C, 170–195 °C, and 240–370 °C, respectively. Moreover, the gel compounds of AH_3 begin to dehydrate at 100 °C and decompose from 210 °C to 370 °C, contributing to further mass loss over this stage [18]. Similar to that of FROPC, 85.53% and 91.62% of the total loss occur before 600 °C, representing the evaporation of most absorbed and bound water. The DTG curve (Fig. 16b) experiences a sudden drop within 600–700 °C due to the dehydration of $C_{12}A_7(H)$ and C–A–(S)–H gels and the corresponding loss of crystalline water [4].

In addition, the DSC curves (Fig. 16b and c) also fluctuate at around 1100 $^{\circ}$C, which is associated with the sintering reaction between $C_{12}A_7$ and amorphous alumina at over 1000 $^{\circ}$C [8].
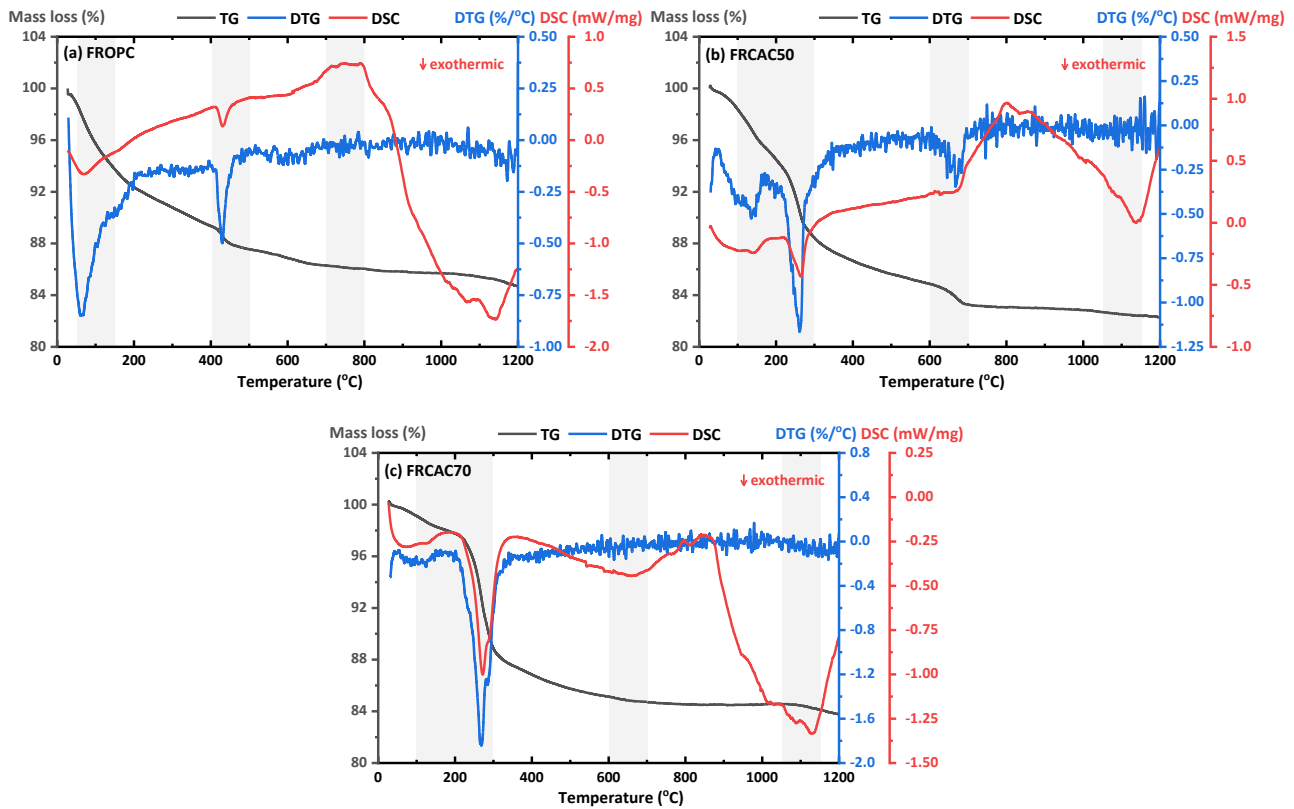

Fig. 16. TG, DTG, and DSC curves of fibre reinforced OPC and CAC samples.

3.6.3. Element distribution

Fig. 17 presents the final distribution of five elements in fibre reinforced samples after exposure to 600 $^{\circ}$C. Regarding the non-metallic elements, the presence of SiO_2 in fine aggregates, hydraulic cement minerals and pozzolanic materials (i.e., micro silica and fly ash) is indicated by the elemental concentrations of Si in all samples, while the elemental concentrations of O are related to the presence of alumina in fine aggregates and the decomposition of hydrated products, including C–S–H gels and CH in OPC (Fig. 17a) as well as C–A–H gels and AH_3 in CAC (Fig. 17b and c). Overall, the variation of cement type and incorporation of SFRP fibres have no significant influence on the distribution of these non-metallic elements.
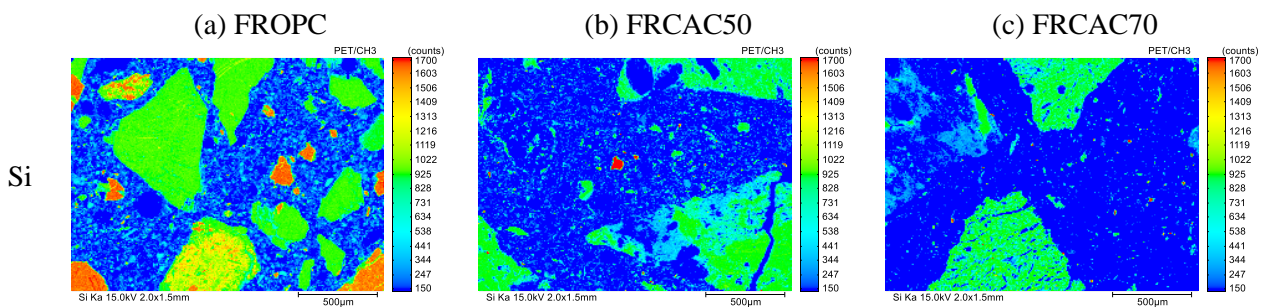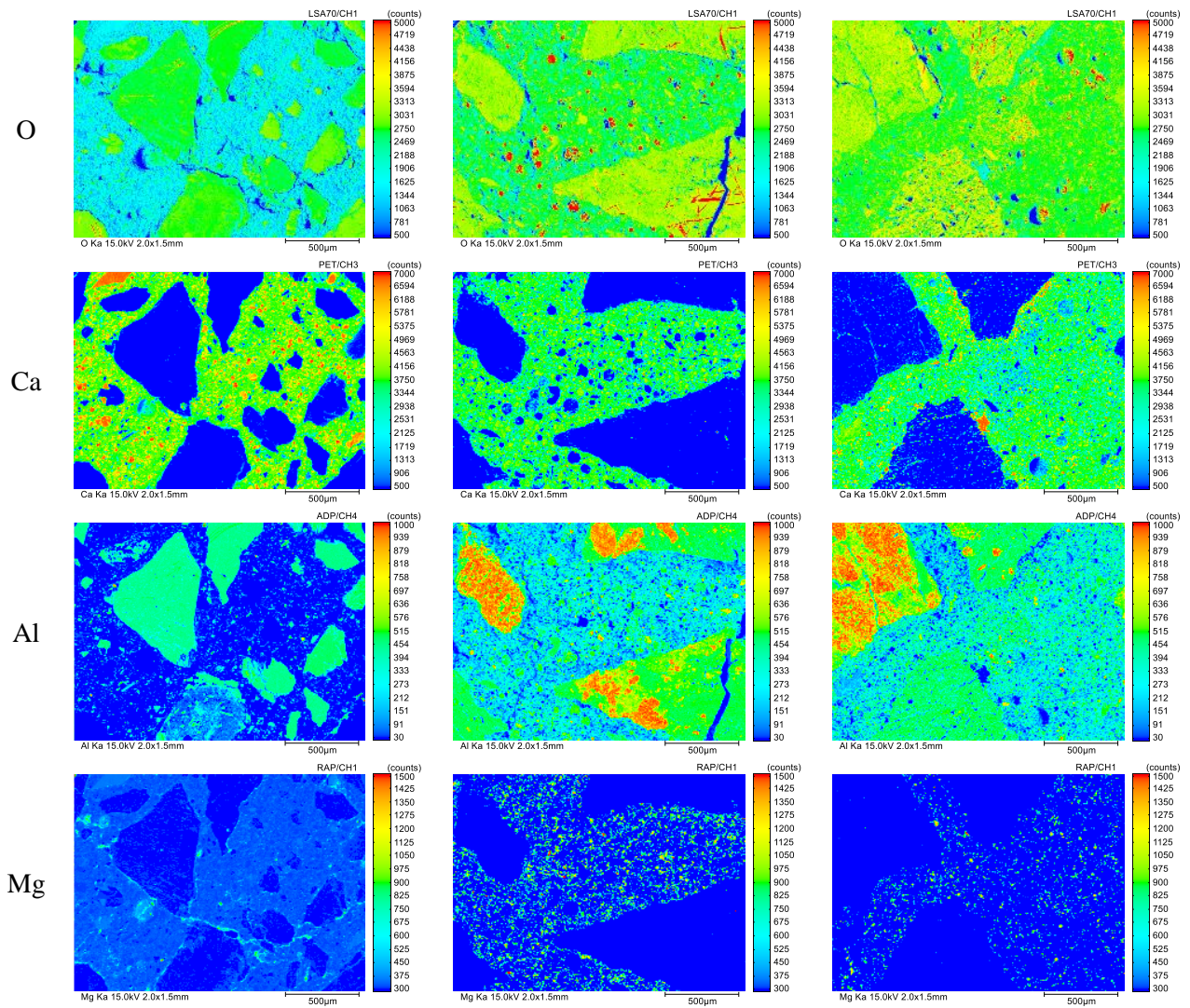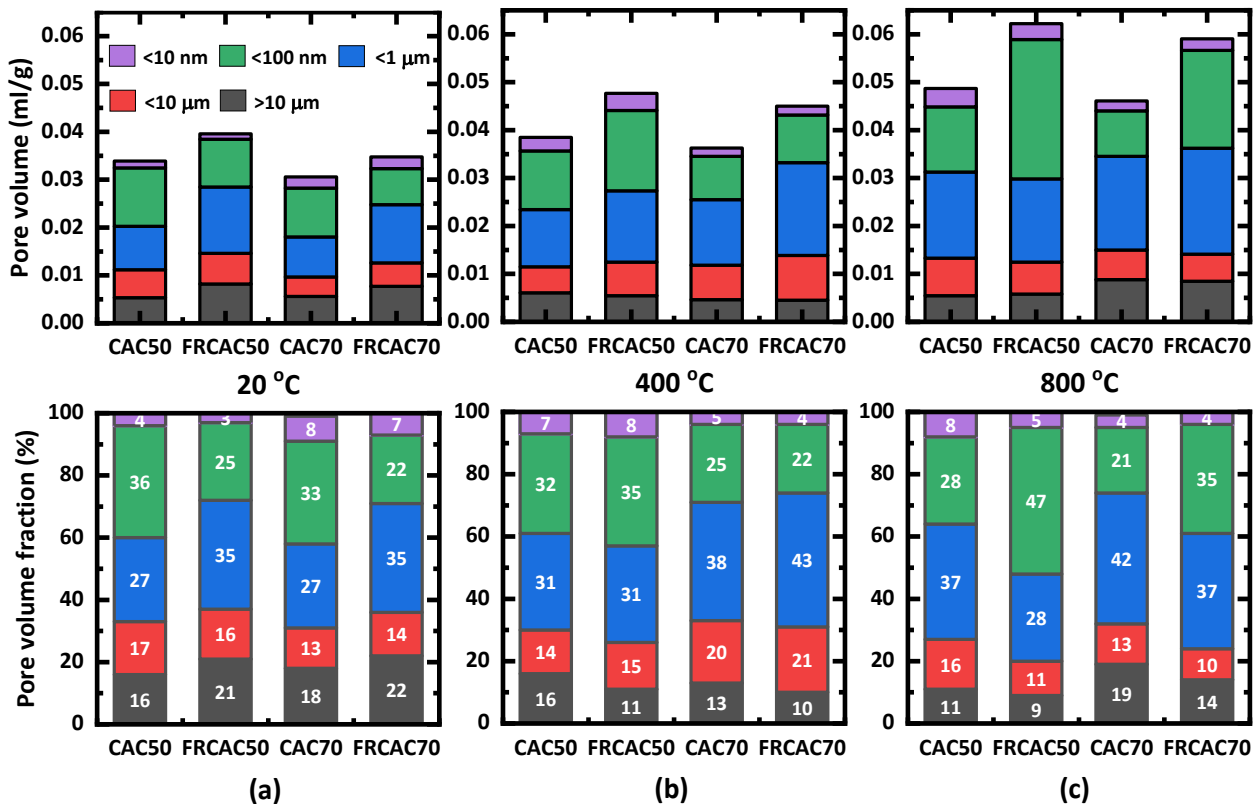
Fig. 17. Element distribution of fibre reinforced OPC and CAC samples after heat exposure.

Regarding the metallic elements, the distribution of Ca is similar in all samples due to the presence of hydrations in cement paste, while the elemental maps of Al and Mg vary a lot between OPC and CAC composites. The elemental concentrations of Al are only present in fine aggregates because of the existence of alumina in aggregates. In contrast, high concentrations of Al also occur in the cement paste of CAC, which can be ascribed to the decomposed products of C–A–H gels and AH_3. Interestingly, a rare concentration of Mg can be detected in Fig. 17a, while the scattered distribution of Mg can be observed in Fig. 17b and c. It is noted that magnesium hydroxide and aluminium hydroxide as two kinds of metallic fillers in SFRP fibres would also decompose at around 500 ºC [30], and their decomposed products would overflow into the concrete matrix through the interconnected pore network, leading to the scattered distribution of Al and Mg in elemental maps. However, the distribution of elements is highly dependent on the observed position, which might result in the variation of Mg concentrations in different samples.

3.6.4. Pore structure

To estimate the effect of SFRP fibres on pore size distribution, the pores are divided into five types based on the diameter, i.e., <10 nm, 10–100 nm, 100–1000 nm, 1–10 µm and >10 µm, referring to

gel pores, meso pores, medium capillary pores, large capillary pores, and macro pores, respectively [5,54]. Fig. 18 illustrates the evolution of pore volume for plain and fibre reinforced CAC samples within different pore ranges. In general, the porosity of CAC increases with temperature while the addition of SFRP further promotes the pore structure of CAC matrix at elevated temperatures. At 20 °C, the porosity of CAC50 is 10.81% higher than that of CAC70, which can be explained by the improved growth of crystalline phases with CA content and thereby results in denser microstructure [8]. The incorporation of 2.0 vol% SFRP fibres leads to a 16.75% and 13.59% increase in the porosity of CAC50 and CAC70, respectively, due to the additional interface transition zones between fibres and concrete [43]. When the temperature increases from 20 °C to 400 °C, the total pore volume of CAC70 rises from 0.0306 ml/g to 0.0361 ml/g, while that of FRCAC70 increases significantly from 0.0347 ml/g to 0.0450 ml/g. On one hand, the conversion reactions of CAH_{10} and C_2AH_8 phases as well as the dehydration of C_3AH_6 and AH_3 crystalline between 120–370 °C result in the loss of bound water and an increase in porosity [14]. On the other hand, the melting of SFRP fibres and foaming of flame retardants would induce micropores/cracks due to the thermal mismatch between embedded fibres and concrete matrix, which helps enhance the connectivity of pore structure [25]. It is noted that the enhancement of pore structure is critical in mitigating the internal pore pressure built up by water evaporation and preventing explosive spalling at elevated temperatures [24]. When the temperature reaches 800 °C, the porosity of FRCAC50 and FRCAC70 shows a 31.19% and 30.48% increase, respectively relative to that at 400 °C, attributed to the synergistic effects of decomposition of amorphous C–A–(S)–H in CAC matrix and thermal expansion of SFRP fibres.

(a) (b) (c)

23

Fig. 18. Pore volume distribution of plain and fibre reinforced OPC and CAC at high temperatures.

The pore volume fraction shown in Fig. 18 provides more insights into the evolution of pore size with temperature. At ambient temperature, meso and medium capillary pores are the two dominant pore ranges in all samples, representing over 57% of the total pore volume. The addition of SFRP fibres leads to the rise in volume fraction of medium capillary and macro pores, while that of meso pores decreases in fibre reinforced samples. This is consistent with a previous study [55] that the incorporation of fibres has an insignificant effect on gel pores, but promotes the formation of large pores. At elevated temperatures, the volume fraction of meso pores in CAC70 drops to only 25% at 400 °C and 21% at 800 °C, in contrast with the significant increase of medium capillary pore fraction to 38% at 400 °C and 42% at 800 °C, indicating that the decomposition of CAC hydrates mainly leads to the formation of medium capillary pores. At elevated temperatures, FRCAC50 has a higher volume fraction of meso pores than that of CAC50, reaching as high as 47% at 800 °C. However, medium capillary pores are the dominant pore ranges in FRCAC70 at all measured temperatures, occupying 43% of the total volume at 400 °C. This suggests that the foaming of SFRP fibres mainly enhances the connectivity of meso pores and medium capillary pores.

Based on the energy conservation theory of MIP measurement, the intruded mercury volume (v_n) and the fractal dimension (D_s) obey the following relationship [56]:

$$\ln\left(\frac{w_n}{r_n^2}\right) = D_s \ln\left(\frac{v_n^{1/3}}{r_n}\right) + C \tag{3}$$

where w_n is the intruded work, r_n denotes the minimum pore diameter, and C is a constant. Fig. 19 demonstrates the scale-dependent fractal dimensions of pore structure in fibre reinforced samples. According to the trend of slope, five fractal regions can be distinguished, i.e., Range I–V, which are consistent with the pore ranges defined by the pore types from gel pore to macro pore. Table 6 further summarises the pore fractal dimension in different fractal ranges. Range I approximately corresponds to the inter-granular pore of C–A–H gels, while Range V is referred to the capillary pore that is directly related to the hydration of CAC binders [57]. Since the polymer fibres do not affect the hydration process [22,25], the addition of fibres has an insignificant effect on pore structure in Ranges I and V. The pore surface areas of FRCAC samples in Ranges II, III, and IV have distinct fractal characteristics with D_s mainly lying within the range of 2–3 [55]. Moreover, the fractal dimension of these ranges satisfies the law Range II>Range III>Range IV, which can be explained by the smaller the pore diameter, the more complicated the spatial distribution of pores. As confirmed by a previous study [58], there is a slight increase in fractal dimension with temperature, attributed to the decomposition of poorly ordered hydration products and foaming of SFRP fibres.
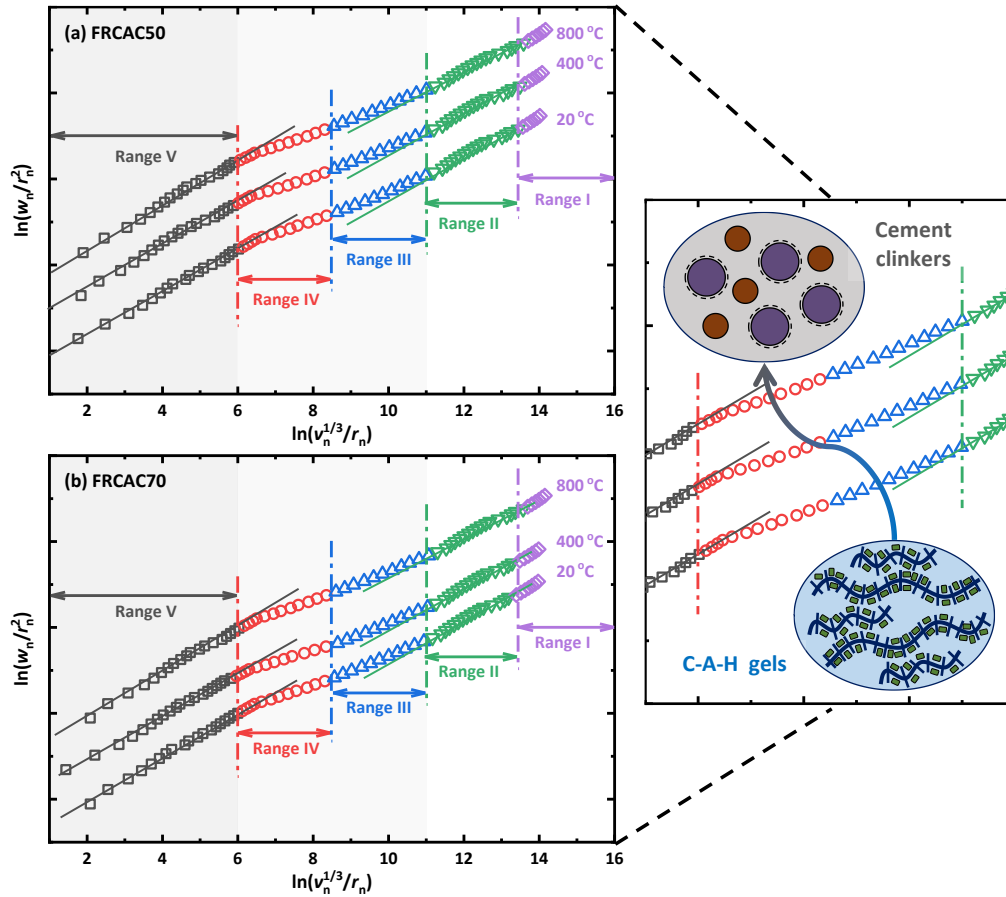
**Fig. 19.** Scale-dependent surface fractal dimension of fibre reinforced CAC in five fractal ranges.

Table 6 Pore surface fractal dimension of fibre reinforced CAC samples at elevated temperatures.

|	Temperature (ºC)	Range I	Range II	Range III	Range IV	Range V
FRCAC50	20	3.173	2.567	2.246	1.922	2.838
	400	3.213	2.697	2.277	2.047	2.921
	800	3.362	2.707	2.342	2.077	2.974
FRCAC70	20	3.084	2.724	2.222	1.907	2.889
	400	3.118	2.784	2.304	2.034	2.988
	800	3.253	2.786	2.309	2.091	3.011

3.7. Micromechanical properties

To characterise the development of micromechanical properties of different phases, nanoindentation tests were performed at 6 different locations of each sample, including fine aggregates, interface transition zones, and cement paste. Fig. 20 shows the measured load-displacement curves for fibre reinforced CAC at 200 ºC and 600 ºC. Based on the dissimilarity in displacement and slope of the unloading portion, the material phases of CAC can be divided into three regions, i.e., ultra-high-density (UHD), high-density (HD), and low-density (LD) phases. The load-displacement curves for UHD phases present the highest slope of unloading portion but the lowest displacement, which indicates the highest elastic modulus and hardness, followed by HD and LD phases. At 200 ºC, the displacement of UHD phases in FRCAC50 varies from 478 nm to 506 nm, while that in FRCAC70 fluctuates between 414 nm and 423 nm. The higher displacement of different phases in FRCAC50 represents lower micromechanical properties as compared with FRCAC70. When the temperature

increases from 200 ℃ to 600 ℃, the displacement of LD phases in FRCAC70 rises from 1412–1572 nm to 1768–1866 nm along with a decrease in slope, indicating the degradation of micromechanical properties with elevated temperatures.
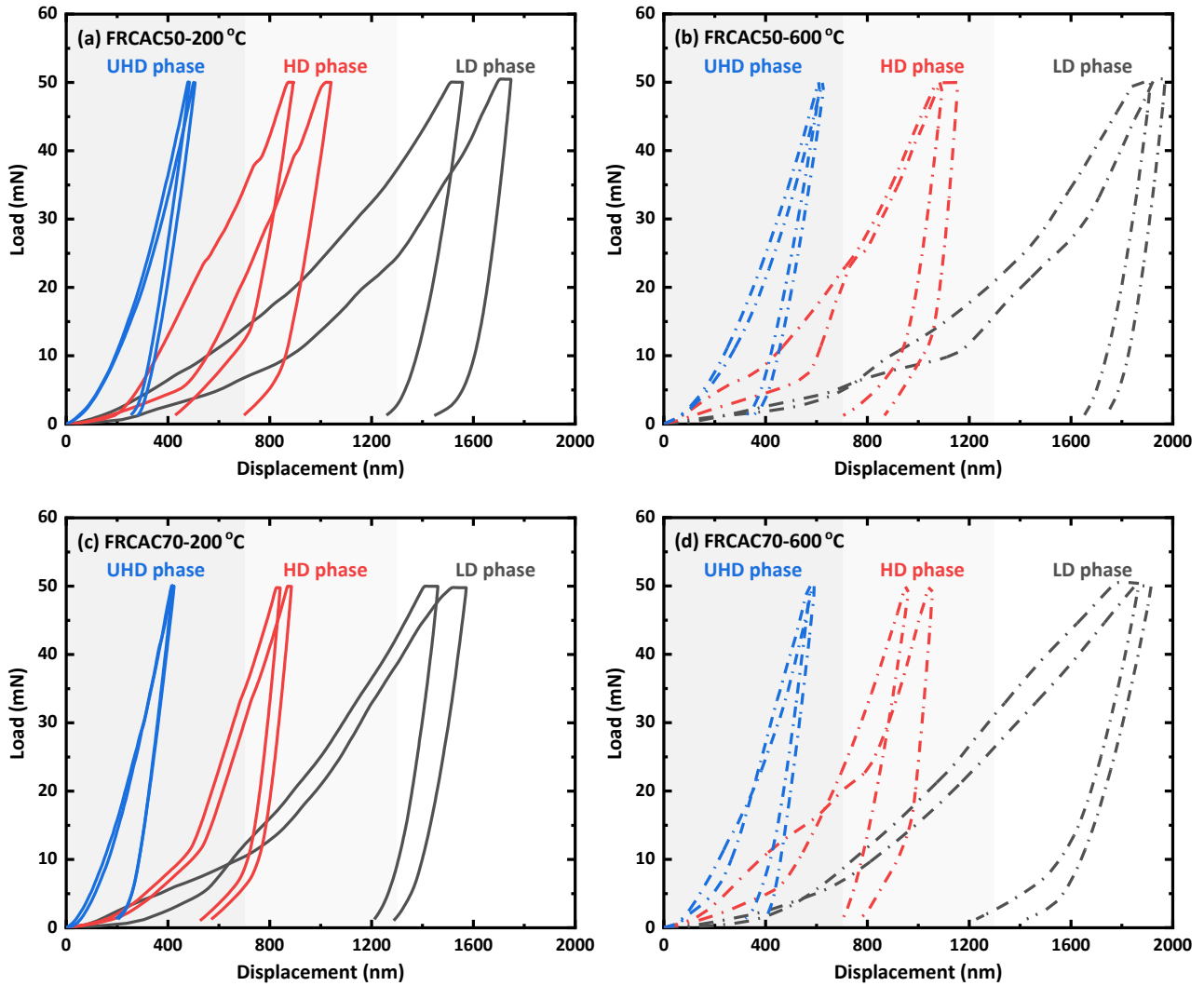
Fig. 20. Load-displacement curves for fibre reinforced CAC at 200 and 600 ℃.
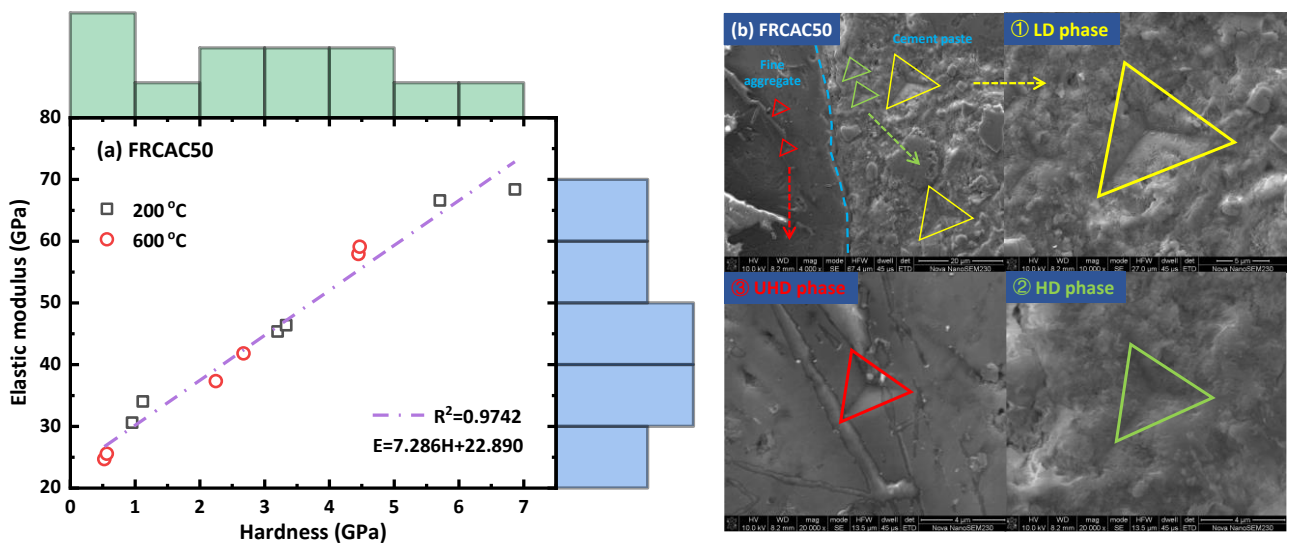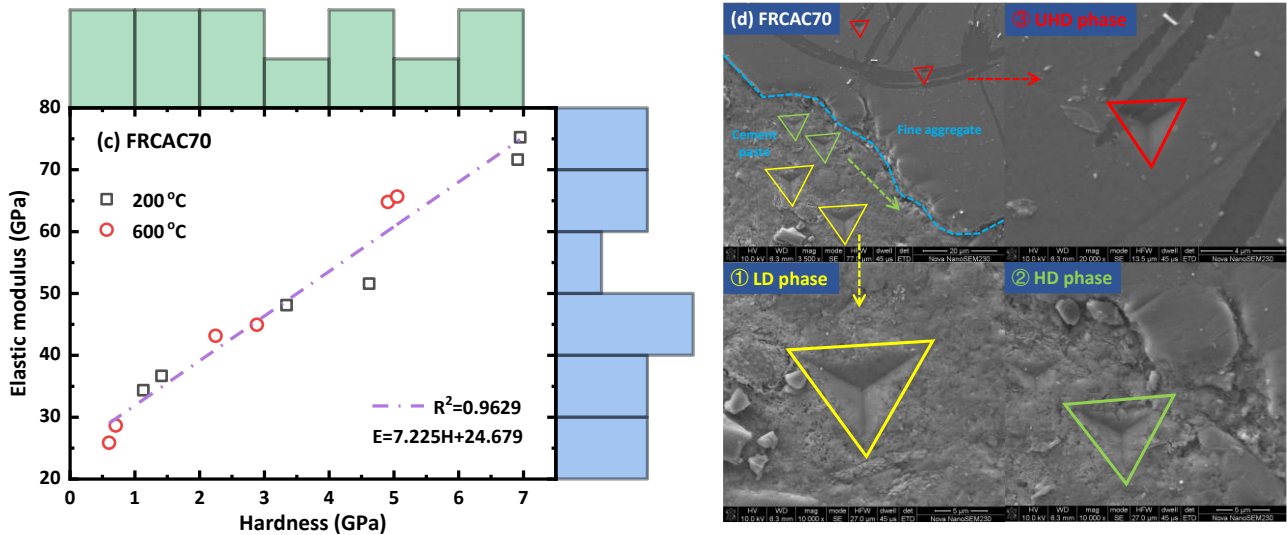
Fig. 21. Relationship between modulus and hardness of fibre reinforced CAC and indent impression.

Based on the measured load-displacement curves, the elastic modulus and hardness of different phases can be obtained, as plotted in Fig. 21. In general, there is a relatively linear relationship between elastic modulus and hardness of material phases, regardless of the temperature. The phases of FRCAC50 show a more rapid increase in elastic modulus with increasing hardness as the slope of fitting curve is slightly higher than that of FRCAC70. However, FRCAC70 performs better in terms of the elastic modulus of material phases under the same hardness. The residual indent impressions presented in Fig. 21b and d also reflect the micromechanical properties of material phases. The shape of indent impression on fine aggregates is an approximately regular triangle with a side length of less than 4 µm, while the largest dimension of residual impression on cement paste reaches more than 10 µm. It is worth noting that even the same type of phases can exhibit different micromechanical behaviour and accordingly the load-displacement response might vary from point to point [59]. From the qualitative perspective, the higher the elastic modulus and hardness of material phases, the smaller the dimension of the corresponding residual indent impressions.

Fig. 22 presents the statistical analysis of elastic modulus and hardness of material phases in plain and fibre reinforced CAC. At 200 ℃, the average elastic modulus and hardness of different phases in CAC70 are 50.83 GPa and 3.92 GPa, respectively, which are 9.08% and 17.28% higher than that of CAC50. This can be ascribed to the enhanced microstructure of concrete induced by higher CA content. The addition of 2.0 vol% SFRP fibres further leads to a 4.14% and 3.55% increase in the average elastic modulus and hardness of different phases in CAC70, indicating that the melting of fibres helps enhance the micromechanical properties. When the temperature reaches 600 ℃, the median elastic modulus and hardness of phases in CAC70 drop to 38.58 GPa and 2.01 GPa, while those of FRCAC70 decrease to 44.06 GPa and 2.57 GPa, respectively. This is because the foaming of SFRP fibres and overflowing of flame-retardant products slow down the heating rate of CAC and thus mitigate the loss of micromechanical properties with increasing temperature. In

addition, the elastic modulus and hardness of material phases are also closely associated with the mechanical properties of CAC, e.g., compressive, tensile, and flexural strengths. The enhanced micromechanical properties of phases due to the physicochemical reactions of SFRP fibres would lead to an improvement in the mechanical properties of CAC at elevated temperatures.
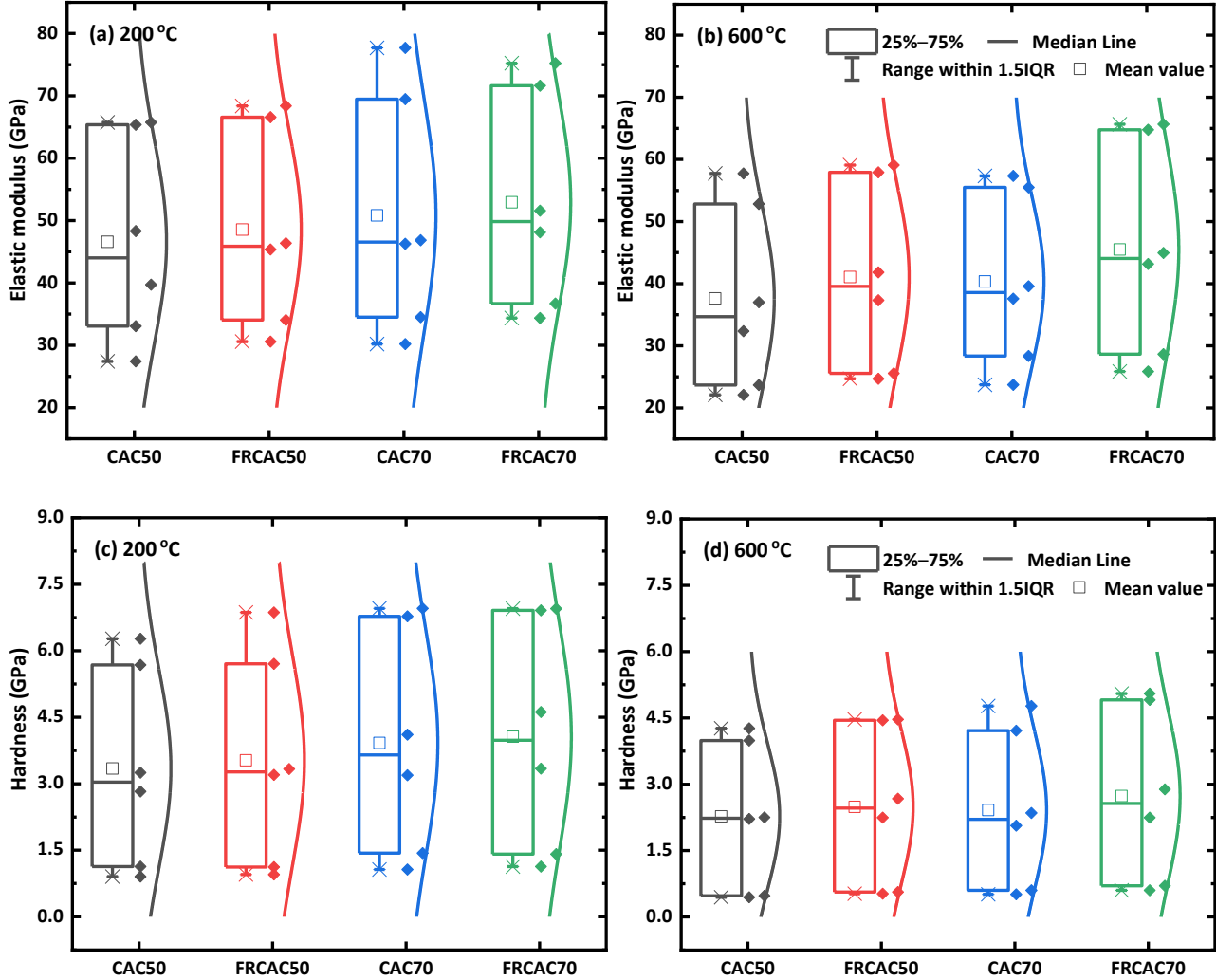

Fig. 22. Elastic modulus and hardness of plain and fibre reinforced CAC by nanoindentation.

4. Discussion

4.1. Thermo-mechanical properties of CAC at elevated temperatures

Towards a better understanding of the mechanism of CAC damage at elevated temperatures, further analysis of the experimental results in terms of thermo-mechanical properties and microstructural evolutions is carried out in comparison with plain OPC (Fig. 23). In general, the damage evolution of CAC is closely related to the moisture transport and physicochemical reactions. At ambient temperature, the setting and hardening of CAC are primarily driven by the hydration of CA, which is highly temperature-dependent and yields the hybrid main hydration products as [8]:

$$CA+10H \rightarrow CAH_{10} \ (T< 20 \ ^{o}C) \tag{4}$$

$$2CA+11H \rightarrow C_2AH_8+AH_3 \ (20 <T< 30 \ ^{o}C) \tag{5}$$
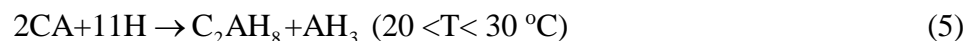
However, the metastable hydrates CAH_{10} and C_2AH_8 would convert to more stable C_3AH_6 with the release of water and consequently alter the mechanical properties through [4]:

$$3CAH_{10} \rightarrow C_3AH_6 + 2AH_3 + 18H \tag{6}$$

$$3C_2AH_8 \rightarrow 2C_3AH_6 + AH_3 + 9H \tag{7}$$

In this study, the XRD patterns (Fig. 15) reveal that the main phases of CAC50 and CAC70 after curing at 20 °C for 28 d are CAH_{10} and C_3AH_6. Although the adverse conversion effect may cause some strength reduction, plain CAC still has higher thermal conductivity and better mechanical properties (i.e., higher compressive, splitting tensile, and bending strengths) than that of plain OPC (Fig. 23a) because of lower porosity and denser microstructure of C–A–H gels [39].
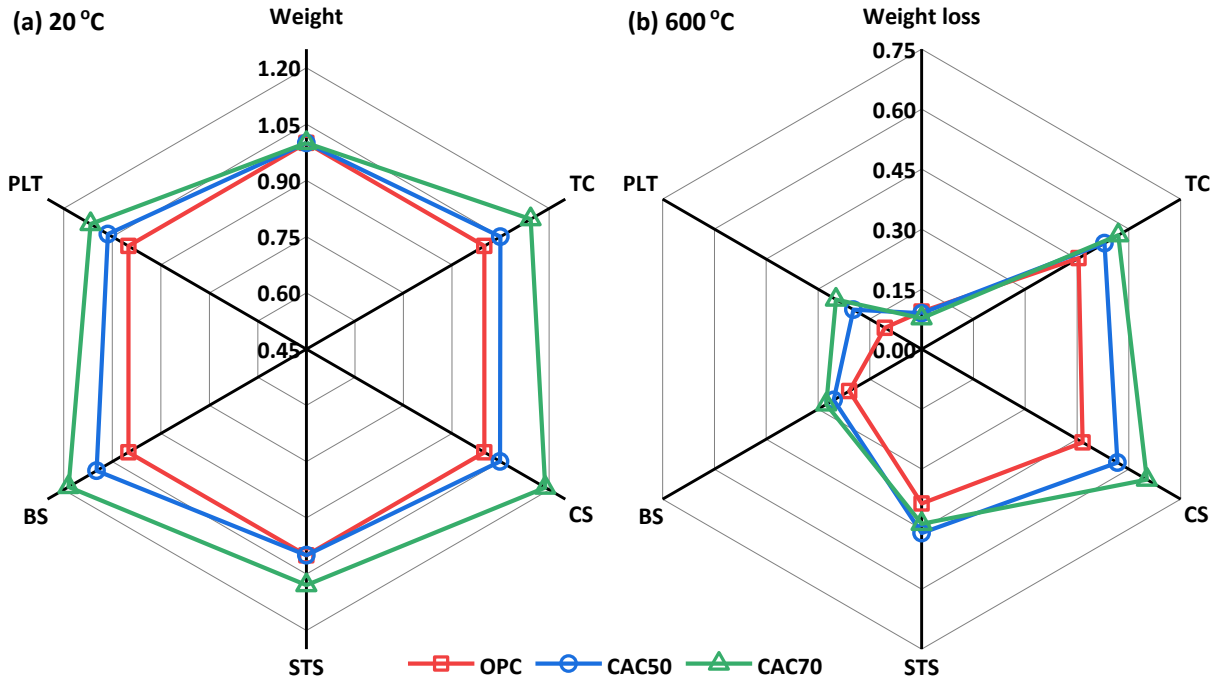
Fig. 23. Comparison of thermo-mechanical properties of OPC and CAC at (a) 20 °C and (b) 600 °C (Note: TC-thermal conductivity, CS-compressive strength, STS-splitting tensile strength, BS-bending strength, PLT-peak-load toughness; TC, CS, STS, BS, and PLT in (a) relative to the values of OPC, while that in (b) compared with the values of them at 20 °C).

Based on TGA and DSC curves (Fig. 16), the physicochemical changes of CAC can be explained at three temperature stages: (i) Stage I (20–200 °C) associated with the dehydration of metastable hydrates and evaporation of free and physically absorbed water; (ii) Stage II (200–400 °C) corresponding to the decomposition of C–A–H and AH_3 gels; (iii) Stage III (400–800 °C) related to the decomposition of C–A–(S)–H phases, as conceptually illustrated in Fig. 24a.

At Stage I, there is continuous weight loss in plain CAC due to the accelerated conversion reactions at over 55 °C and the dehydration of metastable hydrated products (i.e., CAH_{10} and C_2AH_8) from 120 °C to 195 °C [7], which is different from that of plain OPC where a sudden drop in DTG curve occurs at around 100 °C due to the removal of free water (Fig. 16). The loss of free and physically absorbed water and increases in porosity of plain CAC account for over 24.49% of the

total weight loss (Fig. 4) and the approximately 23.46% drop in thermal conductivity (Fig. 5) at this stage. The splitting tensile strength of plain CAC reduces by around 11.81% (Fig. 9), but an over 9.65% increase occurs in compressive strength (Fig. 6) when the temperature increases from 20 $^{\circ}$C to 200 $^{\circ}$C, which can be attributed to the better bonding within interface transition zones by stronger stable hydrations rather than the weaker metastable products [8].

At Stage II, the decomposition of C_3AH_6 at 240–370 $^{\circ}$C and AH_3 at 210–300 $^{\circ}$C results in a further loss of absorbed water and bound water as well as the increase in porosity:

$$4C_3AH_6 + AH_3 \rightarrow 2C_{12}A_7 + 33H \tag{8}$$

Accordingly, there is another 26.11% and 17.26% decrease in weight loss and thermal conductivity of plain CAC over this stage. In addition, all mechanical properties degrade with temperature, while the splitting tensile strength suffers the most with a 28.39% reduction in strength (Fig. 9). However, plain CAC performs better than plain OPC in terms of residual mechanical strength. This can be explained by the reactions between pozzolanic materials and cement clinkers, which helps promote the formation of amorphous C–A–(S)–H phases as confirmed by XRD patterns in Fig. 15 and enhance the mechanical properties of CAC at up to 400 $^{\circ}$C.
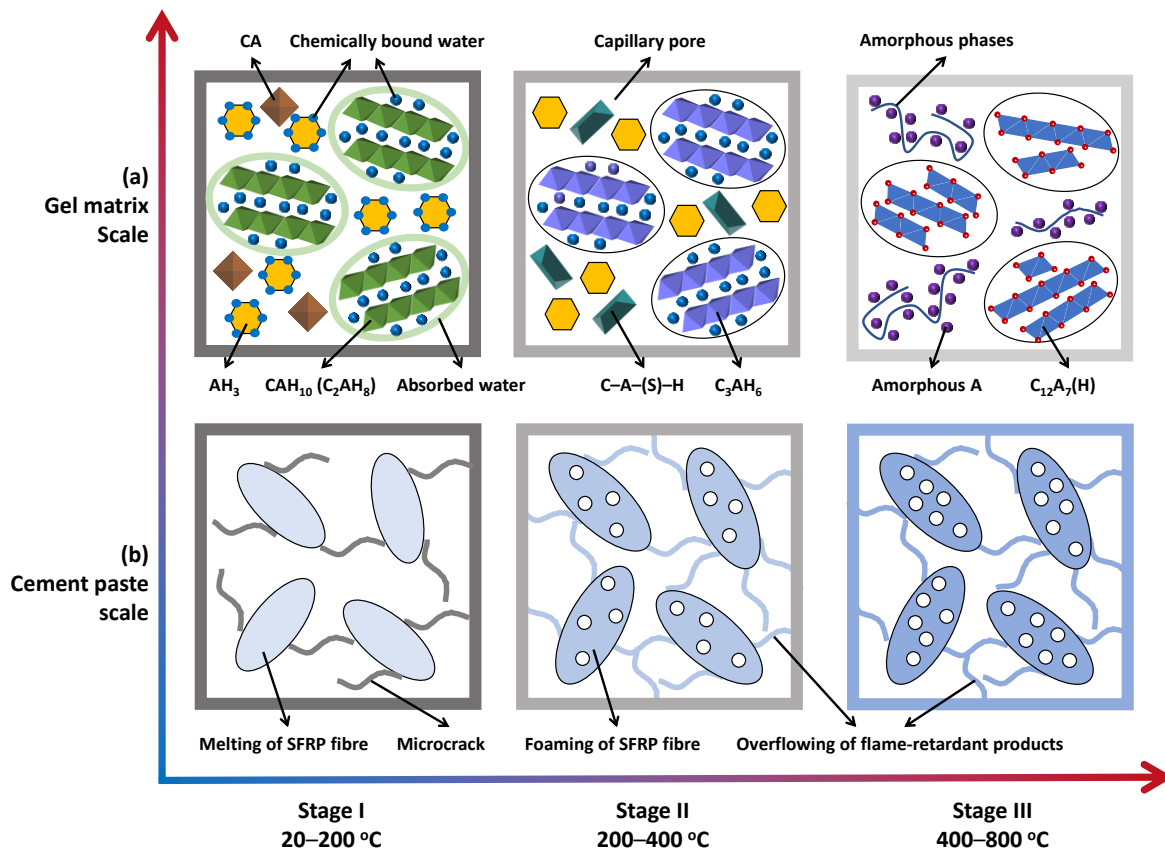
Fig. 24. Schematic illustration of microstructural evolution of SFRP fibre reinforced CAC with temperatures (a) at gel matrix scale and (b) at cement paste scale (Note: A–alumina; C–A–H gels are assumed to be irregular cubic or hexagonal [7,60]).

30

At Stage III, the evaporation of crystalline water in $C_{12}A_7(H)$ and C–A–(S)–H phases results in the loss in weight and conductivity in a similar manner to Stage II. As seen in Fig. 23b, plain CAC has higher compressive, tensile and bending strengths as well as peak-load toughness than that of plain OPC at 600 ^{o}C, while CAC70 even has better strength-sustaining capability in comparison with CAC50. On one hand, OPC is more vulnerable to thermal damage due to the decomposition of C–S–H and CH phases at 120–640 ^{o}C, and the vapour pressure developed by water evaporation can even lead to the explosive spalling (Fig. 11). On the other hand, nearly all gel phases of CAC are dehydrated before reaching 400 ^{o}C, and the dehydrated products are more stable than that of OPC, which reduces swelling risk and exhibits low cracking behaviour [18,39]. The elastic modulus and hardness of materials phases in CAC70 are better than that of CAC50 at up to 600 ^{o}C (Fig. 11), resulting from the promoted mechanical properties with increasing CA content.

4.2. Mechanism of enhanced thermo-mechanical properties of CAC at elevated temperatures

Fig. 25a compares the thermo-mechanical properties of fibre reinforced CAC with that of plain CAC at ambient temperatures. Regarding the thermal property, the incorporation of 2.0 vol% SFRP fibres leads to about 8.95% decrease in thermal conductivity due to the low conducting of SFRP fibres which is less than one-fifth that of the cement hydration, and the enhanced pore structure by additional gaps between SFRP fibres and concrete, especially the increase in medium capillary pores as revealed by MIP (Fig. 18). Regarding mechanical properties, there is an approximately 1.67% drop in compressive strength of fibre reinforced CAC, while the addition of SFRP fibres improves the tensile and bending strengths (Fig. 25a). Generally, polymer fibres would impair the mechanical properties of concrete due to their low modulus, as over 15% strength loss occurs by incorporating only 1.0 vol% PE/PP/PVA fibres [21,23]. However, the high-modulus metallic fillers in polymer resin help improve the mechanical properties (i.e., higher elastic modulus and adhesion) of SFRP fibres [30], which consequently alters the negative effect on strength. Moreover, SFRP fibres also inhibit the initiation and propagation of cracks through the crack-bridging effect and pull-out effect [46,61] and thereby lead to an average of 13.72% increase in peak-load toughness in fibre reinforced CAC, relative to the plain specimens.

The mechanism of enhancing thermo-mechanical properties of CAC at elevated temperatures can also be interpreted using three temperature stages as demonstrated in Fig. 24b. At Stage I, the thermal expansion and melting of SFRP fibres contribute to the enhancement of pore structure and the mitigation of thermal damage. As the polymer matrix of SFRP fibres, PP is characterised by a high coefficient of linear thermal expansion, which increases from 100 µε/^{o}C to 210 µε/^{o}C with the temperature rising from 20 ^{o}C to 140 ^{o}C [38]. Although the thermal expansion of concrete varies with the type and content of aggregates, the expansion coefficient of concrete is still an order of magnitude less than that of PP, i.e., less than 20 µε/^{o}C at up to 300 ^{o}C [62]. The thermal mismatch between embedded fibres and concrete facilitates the formation of interconnected network of cracks

[24], accordingly preventing explosive spalling of concrete (Fig. 11). Moreover, the melting of SFRP fibres at around 165 °C further increases the porosity and provides more channels for water evaporation. At 200 °C, the enhanced pore structure by SFRP fibres leads to a more than 17.30% increase in weight loss (Fig. 4) and approximately 13.79% decrease in thermal conductivity (Fig. 5) of fibre reinforced CAC compared to plain CAC. In addition, FRCAC suffers a 3.81% loss in compressive strength and 1.87% loss in splitting tensile strength (Figs. 6 and 8), relative to plain CAC, as the phase changes soften the SFRP fibres and weaken the pull-out effect. However, the nanoindentation results indicate that the mean elastic modulus and hardness of materials phases of FRCAC are higher than that of plain CAC at 200 °C (Fig. 22). This can be attributed to the low-conducting of pores (an order of magnitude lower than the concrete [34]), which slows down the heat transfer of concrete and then the mechanical degradation.
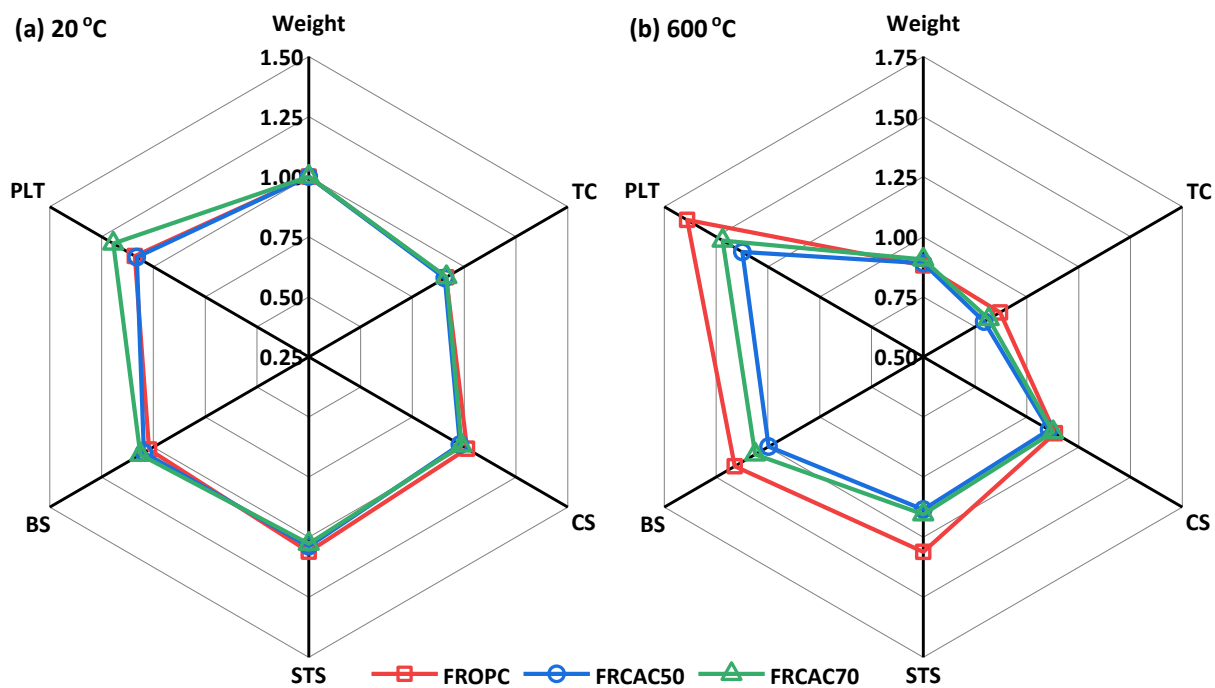
Fig. 25. Comparison of thermo-mechanical properties of FROPC and FRCAC at (a) 20 °C and (b) 600 °C (Note: TC, CS, STS, BS, and PLT in (a) and (b) relative to the values of specimens with plain mixtures at 20 °C and 600 °C, respectively).

At Stage II, the foaming of SFRP fibres further mitigates the thermal damage of CAC by overflowing effect. As per previous studies [63,64], the foaming of intumescent flame retardants in SFRP fibres can be concluded as: (i) ammonium polyphosphate (acid source) begins to decompose at over 220 °C, liberating phosphoric acid and non-flammable gases at the same time; (ii) the resulting acid initiates the dehydration and esterification of pentaerythritol (carbonization agent), triggering a series of subsequent charring reactions from 266 °C to 382 °C; (iii) melamine (spumific agent) starts to decompose at 280–395 °C, producing a large number of porous honeycomb-like foams. It is noted that the decomposition and reaction of these organic flame retardants take place at a similar temperature range, which is favourable to char formation [65]. For fibre reinforced CAC

specimens, the physiochemical reactions of SFRP fibres further enhance the pore structure of concrete, in particular the significant increase in meso pores and medium capillary pores (Fig. 18). As illustrated in Fig. 24b, the flame-retardant foams can overflow to concrete matrix through interconnected cracks (proved by appearance of fibre reinforced specimens in Fig. 11 and element distribution in Fig. 17), which further lower the thermal conductivity of concrete (Fig. 5). As the thermal conductivity is closely associated with the temperature distribution [40], the lower the conductivity, the slower the heating transfer of concrete and thereby the degradation of mechanical properties. Therefore, FRCAC has higher compressive, tensile and bending strengths than plain CAC over this stage (Figs. 6, 8, and 12). For instance, there is a 27.71% increase in peak-load toughness in CAC70 at 300 $^{\circ}$C by incorporating 2.0 vol% SFRP fibres (Table 6).

At Stage III, the commonly used polymer fibres lose their effectiveness due to the evaporation of polymer resin at around 340 $^{\circ}$C [38]. In contrast, the decomposition of magnesium hydroxide and aluminium hydroxide (metallic fillers) in SFRP fibres can still promote the char formation of flame retardants at up to 490 $^{\circ}$C [30]. Driven by the thermal expansion, the resulting flame-retardant foams would even overflow to the surface of concrete through the network of cracks, forming a local insulation layer on the heating surface (Fig. 11). On one hand, the phase changes of SFRP fibres lead to an increased pore volume and fractal dimension within meso and medium capillary pore ranges (Fig. 19), and thus reducing the weight and thermal conductivity of concrete in a similar manner to Stage II. On the other hand, the overflowing effect contributes to mitigating the thermal damage of material phases (Fig. 20). As revealed by nanoindentation results, the median elastic modulus and hardness of individual phases in FRCAC70 are 14.20% and 27.87% higher than that of plain CAC70 at 600 $^{\circ}$C. The improved micromechanical properties of material phases also induce the better mechanical properties, including compressive, splitting tensile and flexural behaviour in comparison with plain CAC, as shown in Fig. 25b. However, it should be mentioned that the phase transformations of SFRP fibres would inevitably affect the crack-bridging effect on tensile and flexural properties. Therefore, hybrid incorporation of SFRP fibres and steel fibres might be an optimal choice for better properties of concrete at elevated temperatures [27,66].

5. Conclusions

In this study, the thermo-mechanical properties of SFRP fibre reinforced CAC at elevated temperatures are experimentally investigated, and the mechanism for mitigating the thermal damage of CAC is explored by microstructural analysis. The main conclusions can be drawn as follows:

- When the temperature reaches 800 $^{\circ}$C, the weight loss of CAC is over 10% of the total mass, while the thermal conductivity reduces by approximately 53.31% of the original value, which can be ascribed to the increase in porosity induced by the evaporation of free, absorbed, and bound water. The addition of 2.0 vol% SFRP fibres further lead to a 23.57% and 18.95% drop in thermal conductivity at 800 $^{\circ}$C, relative to plain CAC50 and CAC70, respectively due to the

enhanced pore structures by phase changes of SFRP fibres.

- The uniaxial compressive strength of CAC reaches a maximum value at 200 $^{\circ}$C, followed by a gradual reduction until 800 $^{\circ}$C, while the splitting tensile strength and flexural properties decrease continuously with increasing temperature. However, the strength loss of CAC is less than that of OPC at elevated temperatures. The residual tensile strength of CAC is over 43.67% at 600 $^{\circ}$C, while that of OPC is only 36.40% compared to the original strength at ambient temperature. The high strength-sustaining capacity of CAC can be attributed to the further hydration between calcium aluminate binders and pozzolanic materials at up to 400 $^{\circ}$C.

- At ambient temperature, SFRP fibres would lead to a slight drop in compressive strength of CAC (about 1.67% with 2.0 vol% fibre), but promote the splitting tensile and bending strengths and peak-load toughness (over 13.72% increase) due to pull-out and crack-bridging effect. Although the melting of SFRP fibres can cause an additional 1.87% tensile strength loss of CAC at 200 $^{\circ}$C, the foaming of SFRP fibres helps mitigate the degradation of CAC at higher temperatures, especially the toughness of FRCAC70 is 1.47 times higher than that of CAC70 at 600 $^{\circ}$C. In addition, the specimens with CA70 binder perform better than those with CA50 binder in terms of mechanical properties due to the improved hydration by alumina.

- The mechanism for enhancing thermo-mechanical properties of CAC can be concluded as: (i) the enhanced connectivity of meso pores and medium capillary pores by thermal expansion and melting of SFRP fibres, and thus improves the permeability of CAC and prevents the explosive spilling; (ii) the overflowing effect of SFRP fibres due to the foaming reactions of metallic-organic flame retardants, which not only lowers the conductivity of concrete matrix but also slows down the degradation of elastic and hardness of material phases with temperature.

Overall, the results indicate a synergistic effect of calcium aluminate binders and SFRP fibres on improving the fire resistance of concrete, making SFRP fibre reinforced CAC a promising sustainable repair material for energy storage and underground constructions. Further research is required to investigate the size effect between fibres and C-A-H phases on thermal conductivity, the temperature dependency of fibre-to-concrete bonding performance, and the effect of hybrid steel and SFRP fibres on thermo-mechanical properties of CAC.

Acknowledgements

References

[1]   M.C.G. Juenger, F. Winnefeld, J.L. Provis, J.H. Ideker, Advances in alternative cementitious

binders, Cem. Concr. Res. 41 (2011) 1232–1243.

[2] Ö. Kirca, I. Özgür Yaman, M. Tokyay, Compressive strength development of calcium aluminate cement-GGBFS blends, Cem. Concr. Compos. 35 (2013) 163–170.

[3] T. Matusinović, J. Šipušić, N. Vrbos, Porosity-strength relation in calcium aluminate cement pastes, Cem. Concr. Res. 33 (2003) 1801–1806.

[4] N.Y. Mostafa, Z.I. Zaki, O.H. Abd Elkader, Chemical activation of calcium aluminate cement composites cured at elevated temperature, Cem. Concr. Compos. 34 (2012) 1187–1193.

[5] W. Ding, Y. He, L. Lu, F. Wang, S. Hu, Mechanical property and microstructure of quaternary phase paste blended with metakaolin, Cem. Concr. Compos. 118 (2021) 103934.

[6] M. Idrees, O. Ekincioglu, M.S. Sonyal, Hydration behavior of calcium aluminate cement mortars with mineral admixtures at different curing temperatures, Constr. Build. Mater. 285 (2021) 122839.

[7] X. Cheng, Q. Dong, Y. Ma, C. Zhang, X. Gao, Y. Yu, Z. Wen, C. Zhang, X. Guo, Mechanical and thermal properties of aluminate cement paste with blast furnace slag at high temperatures, Constr. Build. Mater. 228 (2019) 116747.

[8] D.A. Strauss Rambo, N. Ukrainczyk, F. de Andrade Silva, E. Koenders, R.D. Toledo Filho, O. da Fonseca Martins Gomes, Calcium-aluminate mortars at high temperatures: Overcoming adverse conversion effects using clinker aggregates, Cem. Concr. Compos. 96 (2019) 212–224.

[9] D.A. Strauss Rambo, F. De Andrade Silva, R.D. Toledo Filho, N. Ukrainczyk, E. Koenders, Tensile strength of a calcium-aluminate cementitious composite reinforced with basalt textile in a high-temperature environment, Cem. Concr. Compos. 70 (2016) 183–193.

[10] J.H. Ideker, K.L. Scrivener, H. Fryda, B. Touzo, Calcium aluminate cements, 2019.

[11] T. Pyatina, T. Sugama, Acid resistance of calcium aluminate cement-fly ash F blends, Adv. Cem. Res. 28 (2016) 433–457.

[12] K.L. Scrivener, J.L. Cabiron, R. Letourneux, High-performance concretes from calcium aluminate cements, Cem. Concr. Res. 29 (1999) 1215–1223.

[13] Q. Jin, S.L. Hordern, Y. Tang, K.E. Kurtis, NOx sequestration by calcium aluminate cementitious materials, Cem. Concr. Res. 142 (2021) 106381.

[14] N.K. Lee, K.T. Koh, S.H. Park, G.S. Ryu, Microstructural investigation of calcium aluminate cement-based ultra-high performance concrete (UHPC) exposed to high temperatures, Cem. Concr. Res. 102 (2017) 109–118.

[15] Y. Li, Effect of post-fire curing and silica fume on permeability of ultra-high performance concrete, Constr. Build. Mater. 290 (2021) 20–22.

[16] G.F. Peng, X.J. Niu, Y.J. Shang, D.P. Zhang, X.W. Chen, H. Ding, Combined curing as a

novel approach to improve resistance of ultra-high performance concrete to explosive spalling under high temperature and its mechanical properties, Cem. Concr. Res. 109 (2018) 147–158.

[17] P.R. Prem, B.H. Bharatkumar, A.R. Murthy, Influence of curing regime and steel fibres on the mechanical properties of UHPC, Mag. Concr. Res. 67 (2015) 988–1002.

[18] M. Roig-Flores, T. Lucio-Martin, M.C. Alonso, L. Guerreiro, Evolution of thermo-mechanical properties of concrete with calcium aluminate cement and special aggregates for energy storage, Cem. Concr. Res. 141 (2021) 106323.

[19] Q. Zeng, R. Fang, H. Li, Y. Peng, J. Wang, Tailoring the thermal and mechanical properties of lightweight cement-based composites by macro and micro fillers, Cem. Concr. Compos. 102 (2019) 169–184.

[20] M. Yoon, G. Kim, G.C. Choe, Y. Lee, T. Lee, Effect of coarse aggregate type and loading level on the high temperature properties of concrete, Constr. Build. Mater. 78 (2015) 26–33.

[21] J.J. Park, D.Y. Yoo, S.S.W. Kim, S.S.W. Kim, Benefits of synthetic fibers on the residual mechanical performance of UHPFRC after exposure to ISO standard fire, Cem. Concr. Compos. 104 (2019) 103401.

[22] M. Chen, Z.H. Sun, W.L. Tu, X. Yan, M.Z. Zhang, Behaviour of recycled tyre polymer fibre reinforced concrete at elevated temperatures, Cem. Concr. Compos. 124 (2021) 104257.

[23] S. Sanchayan, S.J. Foster, High temperature behaviour of hybrid steel–PVA fibre reinforced reactive powder concrete, Mater. Struct. 49 (2016) 769–782.

[24] D. Zhang, A. Dasari, K.H. Tan, On the mechanism of prevention of explosive spalling in ultra-high performance concrete with polymer fibers, Cem. Concr. Res. 113 (2018) 169–177.

[25] D. Zhang, K.H. Tan, Effect of various polymer fibers on spalling mitigation of ultra-high performance concrete at high temperature, Cem. Concr. Compos. 114 (2020) 103815.

[26] Y. Li, P. Pimienta, N. Pinoteau, K.H. Tan, Effect of aggregate size and inclusion of polypropylene and steel fibers on explosive spalling and pore pressure in ultra-high-performance concrete (UHPC) at elevated temperature, Cem. Concr. Compos. 99 (2019) 62–71.

[27] Y. Zhu, H. Hussein, A. Kumar, G. Chen, A review: Material and structural properties of UHPC at elevated temperatures or fire conditions, Cem. Concr. Compos. 123 (2021) 104212.

[28] J. Tang, W. Ma, Y. Pang, J. Fan, D. Liu, L. Zhao, S. Ahmed Sheikh, Uniaxial compression performance and stress–strain constitutive model of the aluminate cement-based UHPC after high temperature, Constr. Build. Mater. 309 (2021) 125173.

[29] T. Zhang, Y. Zhang, Z. Xiao, Z. Yang, H. Zhu, J.W.W. Ju, Z. Yan, Development of a novel bio-inspired cement-based composite material to improve the fire resistance of engineering structures, Constr. Build. Mater. 225 (2019) 99–111.

[30] T. Zhang, M. Zhang, Y. Shen, H. Zhu, Z. Yan, Mitigating the damage of ultra-high performance concrete at elevated temperatures using synergistic flame-retardant polymer fibres, Cem. Concr. Res. 158 (2022) 106835.

[31] Z. Wang, E. Han, W. Ke, Effect of nanoparticles on the improvement in fire-resistant and anti-ageing properties of flame-retardant coating, Surf. Coatings Technol. 200 (2006) 5706–5716.

[32] J.Z. Liang, J.Q. Feng, C.P. Tsui, C.Y. Tang, D.F. Liu, S.D. Zhang, W.F. Huang, Mechanical properties and flame-retardant of PP/MRP/Mg(OH)$_2$/Al(OH)$_3$ composites, Compos. Part B Eng. 71 (2015) 74–81.

[33] GB/T 50081, Chinese code for test methods of concrete physical and mechanical properties, Beijing, (2019).

[34] T. Zhang, Y. Zhang, H. Zhu, Z. Yan, Experimental investigation and multi-level modeling of the effective thermal conductivity of hybrid micro-fiber reinforced cementitious composites at elevated temperatures, Compos. Struct. 256 (2021) 112988.

[35] C. Rocco, G. V. Guinea, J. Planas, M. Elices, Review of the splitting-test standards from a fracture mechanics point of view, Cem. Concr. Res. 31 (2001) 73–82.

[36] ASTM C 1609/C 1609M-12, Structural test method for flexural performance of fiber reinforced concrete (using beam with third point loading), American Society of Testing and Materials, (2012).

[37] H. Ma, Mercury intrusion porosimetry in concrete technology: Tips in measurement, pore structure parameter acquisition and application, J. Porous Mater. 21 (2014) 207–215.

[38] G.A. Khoury, B. Willoughby, Polypropylene fibres in heated concrete. Part 1: Molecular structure and materials behaviour, Mag. Concr. Res. 60 (2008) 125–136.

[39] W. Khaliq, H.A. Khan, High temperature material properties of calcium aluminate cement concrete, Constr. Build. Mater. 94 (2015) 475–487.

[40] T. Zhang, Y. Zhang, H. Zhu, Z. Yan, Characterizing the thermal properties of hybrid polypropylene-steel fiber reinforced concrete under heat exposure: Insights into fiber geometry and orientation distribution, Compos. Struct. 275 (2021) 114457.

[41] A.S. Tolkacheva, P.A. Popov, S.N. Shkerin, S. V. Naumov, P.D. Khavlyuk, A.A. Krugovykh, S. V. Telegin, Thermal conductivity of calcium aluminate and complex vanadates of garnet structure, Russ. J. Appl. Chem. 93 (2020) 325–332.

[42] M. Javad, A. Qomi, F. Ulm, R.J. Pellenq, Physical origins of thermal properties of cement paste, Phys. Rev. Appl. 3 (2015) 064010.

[43] M. Zeiml, D. Leithner, R. Lackner, H.A. Mang, How do polypropylene fibers improve the spalling behavior of in-situ concrete, Cem. Concr. Res. 36 (2006) 929–942.

[44] N. Ukrainczyk, T. Matusinovi, Thermal properties of hydrating calcium aluminate cement

pastes, Cem. Concr. Res. 40 (2010) 128–136.

[45] Y. Luo, K.M. Klima, H.J.H. Brouwers, Q. Yu, Effects of ladle slag on Class F fly ash geopolymer: Reaction mechanism and high temperature behavior, Cem. Concr. Compos. (2022) 104468.

[46] Y. Zhang, J.W. Ju, Q. Chen, Z. Yan, H. Zhu, Characterizing and analyzing the residual interfacial behavior of steel fibers embedded into cement-based matrices after exposure to high temperatures, Compos. Part B. 191 (2020) 107933.

[47] M.F.M. Zain, H.B. Mahmud, A. Ilham, M. Faizal, Prediction of splitting tensile strength of high-performance concrete, Cem. Concr. Res. 32 (2002) 1251–1258.

[48] X. Hou, P. Ren, Q. Rong, W. Zheng, Y. Zhan, Effect of fire insulation on fire resistance of hybrid-fiber reinforced reactive powder concrete beams, Compos. Struct. 209 (2019) 219–232.

[49] F. Liu, W. Ding, Y. Qiao, Experimental investigation on the flexural behavior of hybrid steel-PVA fiber reinforced concrete containing fly ash and slag powder, Constr. Build. Mater. 228 (2019) 116706.

[50] Y. Li, E.-H.E.H. Yang, K.H. Tan, Flexural behavior of ultra-high performance hybrid fiber reinforced concrete at the ambient and elevated temperature, Constr. Build. Mater. 250 (2020) 118487.

[51] ASTM C 1018-97, Standard test method for flexural toughness and first-crack strength of fiber-reinforced concrete (using beam with third-point loading), (1997).

[52] G.A. Khoury, Effect of fire on concrete and concrete structures, Prog. Struct. Eng. Mater. 2 (2000) 429–447.

[53] F.A. Cardoso, M.D.M. Innocentini, M.M. Akiyoshi, V.C. Pandolfelli, Effect of curing time on the properties of CAC bonded refractory castables, J. Eur. Ceram. Soc. 24 (2004) 2073–2078.

[54] Q. Zeng, K. Li, T. Fen-chong, P. Dangla, Pore structure characterization of cement pastes blended with high-volume fly ash, Cem. Concr. Res. 42 (2012) 194–204.

[55] D. Li, D. Niu, Q. Fu, D. Luo, Fractal characteristics of pore structure of hybrid Basalt-Polypropylene fibre-reinforced concrete, Cem. Concr. Compos. 109 (2020) 103555.

[56] B. Zhang, S. Li, Determination of the surface fractal dimension for porous media by mercury prosimetry, Ind. Eng. Chem. Res. 34 (1995) 1383–1386.

[57] Q. Zeng, M. Luo, X. Pang, L. Li, K. Li, Surface fractal dimension: An indicator to characterize the microstructure of cement-based porous materials, Appl. Surf. Sci. 282 (2013) 302–307.

[58] L. Li, Z. Li, M. Cao, Y.I. Tang, Z.H.E. Zhang, Nanoindentation and porosity fractal dimension of calcium carbonate whisker reinforced cement paste after elevated temperatures

(up to 900 °C), Fractals. 29 (2021) 2140001.

[59] G. Fang, M. Zhang, Multiscale micromechanical analysis of alkali-activated fly ash-slag paste, Cem. Concr. Res. 135 (2020) 106141.

[60] R.C. Ivanov, C. Angulski da Luz, H.E. Zorel, J.I. Pereira Filho, Behavior of calcium aluminate cement (CAC) in the presence of hexavalent chromium, Cem. Concr. Compos. 73 (2016) 114–122.

[61] S. Dong, Y. Wang, A. Ashour, B. Han, J. Ou, Nano/micro-structures and mechanical properties of ultra-high performance concrete incorporating graphene with different lateral sizes, Compos. Part A Appl. Sci. Manuf. 137 (2020) 106011.

[62] G.A. Khoury, Strain of heated concrete during two thermal cycles. Part 1: Strain over two cycles, during first heating and at subsequent constant temperature, Mag. Concr. Res. 58 (2006) 367–385.

[63] Z. Wang, E. Han, W. Ke, Effect of acrylic polymer and nanocomposite with nano-SiO2 on thermal degradation and fire resistance of APP-DPER-MEL coating, Polym. Degrad. Stab. 91 (2006) 1937–1947.

[64] J. Gu, G. Zhang, S. Dong, Q. Zhang, J. Kong, Study on preparation and fire-retardant mechanism analysis of intumescent flame-retardant coatings, Surf. Coatings Technol. 201 (2007) 7835–7841.

[65] S. Zhou, L. Song, Z. Wang, Y. Hu, W. Xing, Flame retardation and char formation mechanism of intumescent flame retarded polypropylene composites containing melamine phosphate and pentaerythritol phosphate, Polym. Degrad. Stab. 93 (2008) 1799–1806.

[66] Y. Li, K.H. Tan, E.H. Yang, Synergistic effects of hybrid polypropylene and steel fibers on explosive spalling prevention of ultra-high performance concrete at elevated temperature, Cem. Concr. Compos. 96 (2019) 174–181.